Bulletin of Micro and Nanoelectrotechnologies

March 2012, vol. III, no. 1

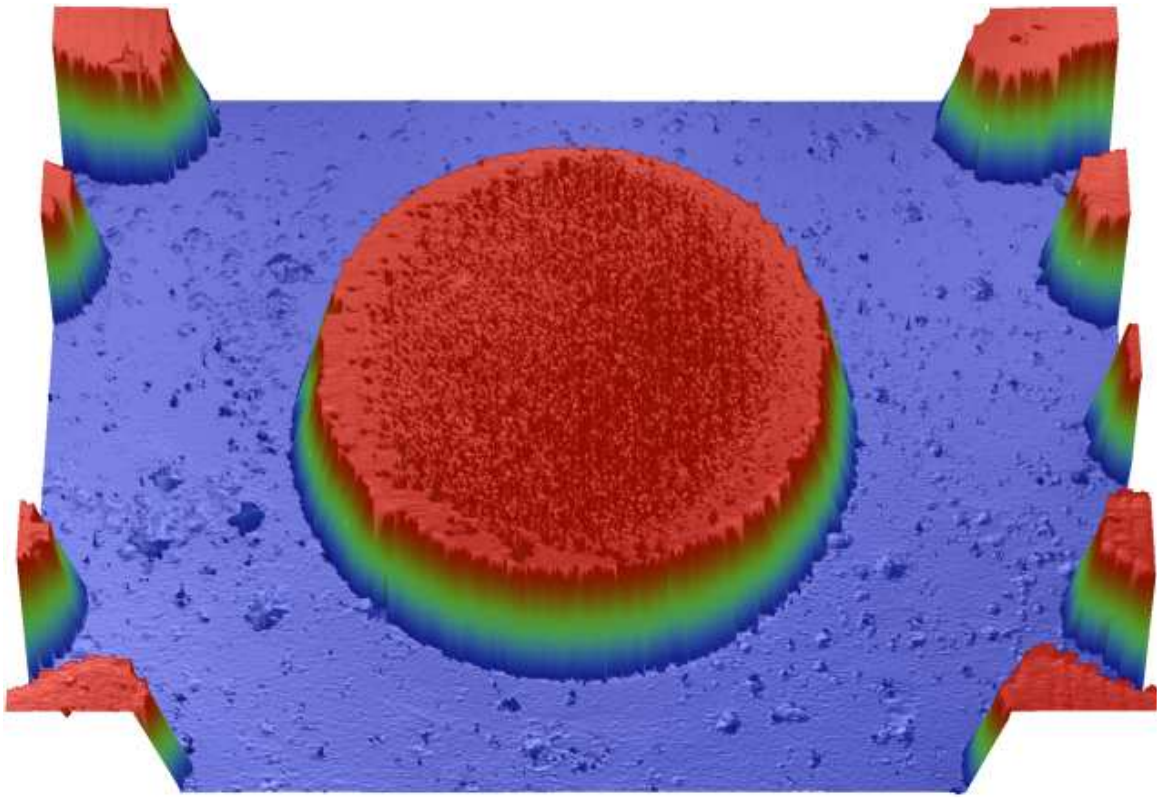

A publication of the Micro and Nanoelectrotechnologies Department of National Research and Development Institute for Electrical Engineering-Advanced Research

Editorial Board

ISSN 2069-1505

Manuscript submission

The Guest Editors will send the manuscripts by post or to the e-mail: mignat@icpe-ca.ro

Contact e-mail: ghristea@icpe-ca.ro

Address:

Splaiul Unirii No. 313, sect. 3, Bucharest-030138 - Romania

Our staff will contact the Guest Editors in order to arrange future actions concerning manuscripts.

Bulletin of Micro and Nanoelectrotechnologies includes the specific research studies on:

- Microelectromechanical and nanoelectromechanical components.
- The typical micro and nanostructure of actuators, micromotors and sensors.
- The harvesting microsystems.
- The conventional and unconventional technologies on MEMS and NEMS.
- The theoretical and experimental studies on electric, magnetic or electromagnetic field with applications on micro and nano actuating and sensing effects.
- The design algorithms or procedures of MEMS and NEMS components.
- The applications of MEMS and NEMS in biology and in biomedical field.
- The new materials in MEMS and NEMS.
- The standardization and reliability preoccupations.
- The economic and financial analysis and evolutions of MEMS and NEMS specific markets.

Contents

The Impedance Cardiography for Blood Flow Properties Monitoring

[*]Alin Alexandru Dobre, [*]Corina Mihaela Ipate, [*,**]Alexandru Mihail Morega
[*]University POLITEHNICA of Bucharest, Faculty of Electrical Engineering, Splaiul Independentei no. 313, 060042, Bucharest, Romania
[**]"Gheorghe Mihoc – Caius Iacob" Institute of Statistical Mathematics and Applied Mathematics, Romanian Academy, Calea 13 Septembrie no.13, 050711, Bucharest, Romania.
alin.dobre@iem.pub.ro, ipate.mcorina@gmail.com, amm@iem.pub.ro

Abstract – This paper presents numerical simulation and experimental results on the impedance cardiography (ICG) and electric cardiometry (EC) non-invasive procedures used for investigation and monitoring of hemodynamic properties. Our numerical models rely on realistic, patient-related reconstructed computational domains, produced out of high resolution CT (computed tomography) image datasets. ICG measurements were also conducted on twelve subjects and the results are presented and discussed here.

***Index Terms* – Impedance cardiography, impedance cardiometry, numerical simulation, CT image reconstruction.**

I. INTRODUCTION

Studies of the impedance cardiography (ICG), known for more than fifty years, mention this technique as a method of measuring systolic time intervals and cardiac output [1]. The ICG and the electric *cardiometry*[1] (EC) are simple, noninvasive and inexpensive hemodynamic monitoring methods for measuring the properties of the blood flow in the thorax, using the electrical conductivity property of the blood [1,3].

Some of the most important applications of the impedance cardiography methods are in patient assessment, selecting pharmacological agents and adjusting the dosages, optimization of pacemaker settings and monitoring patients' response to therapy. The full list of the parameters that can be evaluated using the ICG and the EC techniques is included in Table III. These methods use a low-amplitude, high frequency alternating signal (50-100 kHz) to determine the chest blood flow impedance. Important hemodynamic parameters, such as the stroke volume (*SV*) and the cardiac output (*CO*), can be further derived [2]. *SV* echoes the volume of blood pumped by the left ventricle at each contraction, while *CO* is the total volume of blood pumped by the ventricle per minute.

ICG and EC rely on Ohm's law applied to the thoracic equivalent electric circuit. The changes in voltage and electrical resistance are related to hemodynamic parameters of the cardiac function. Usually, the ICG waveform, which reveals pathological behaviors in the mechanical activity of the heart, is correlated significantly to the electrocardiography (ECG) waveform that, in turn, highlights the electrical activity of the heart, in order to provide for a more accurate and meaningful investigation results (Fig. 1).

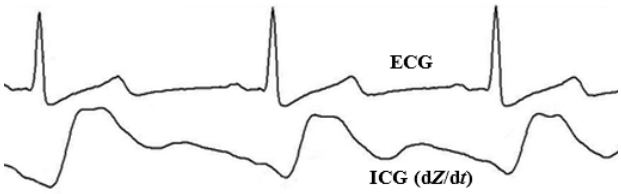

Fig. 1. Correlated electrocardiography (ECG) and impedance cardiography (ICG) waveforms [1].

The main difference between the ICG and EC noninvasive investigations resides in what concerns the cardiac output (*CO*) level: the ICG isn't approved for usage in patients with low *COs* (*e.g.*, children and neonates), while EC doesn't meet any of these limitations.

II. THE ICG AND ELECTRICAL CARDIOMETRY METHODS

The ICG evaluates the heartbeat related changes of thoracic bioimpedance via four sensors (electrodes) placed on the neck and thorax. An alternating electrical current of low (100 μA RMS value), constant amplitude is injected through the "current" electrodes [4].

The voltage drop, acquired through "voltage" electrodes that are conveniently placed on the thorax provides for a measure of the associated electric field in the anatomic structure (Fig. 2). The output voltage is used to define the biological

[1] Cardiometry technique is a trademark of Cardiotronic Inc.

impedance $Z(t)$: when the electrical current value is kept constant, the output voltage is proportional to $Z(t)$. In this case, the biological equivalent system does not include either inductive or capacitive elements, so the impedance is purely resistive [5].

Due to the high values of the electrical conductivity of the blood, as compared to the surrounding thoracic tissues, the effective *SV* is mainly influenced by the blood pulsation in the blood vessels of greater diameters [6]. Thus, the changes in $Z(t)$ occurring with every heartbeat outline the *SV*.

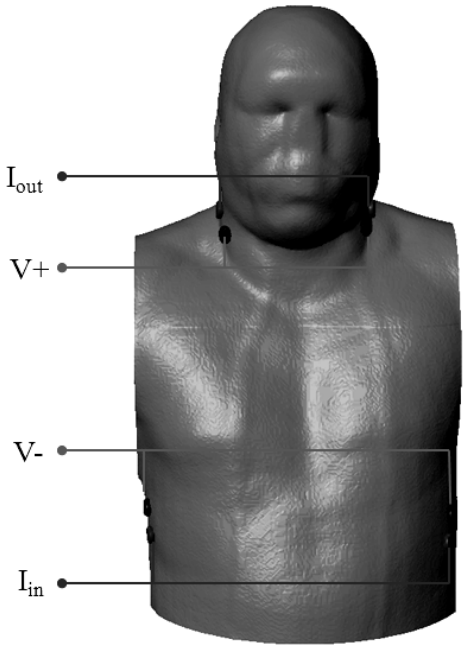

Fig. 2. Electrode setup for the ICG technique.

The expression that correlates the change in impedance ΔZ and the base impedance Z_0 to the volume change ΔV of the thorax is given by [7]

$$\Delta V = \rho \frac{L^2}{Z_0^2} \Delta Z, \qquad (1)$$

where ρ [$\Omega \cdot$m] is the electrical resistivity of blood, and L [m] the distance between the electrodes.

Assuming the cylindrical conductor model for the chest, Kubicek *et al.* [1,2] introduced a definition for *SV* that includes the maximum value of the time derivative of the impedance waveform $(dZ/dt)_{max}$

$$SV = \rho \frac{L^2}{Z_0^2} \left(\frac{dZ}{dt} \right)_{max} \cdot LVET, \qquad (2)$$

where *LVET* [s] is the left ventricular ejection time, and $(dZ/dt)_{max}$ is the module of the maximum change rate (slope) in the impedance waveform per beat [Ω/s].

Sramek *et al.* [7] defined an expression for *SV* that replaces the conductor model used by Kubicek with a truncated cone. In this case, the size L is approximated as 17% of the patient's height H, yielding

$$SV = LVET \cdot \frac{(0.17H)^3}{4.2} \cdot \left(\frac{dZ}{dt} \right)_{max} \Big/ Z_0. \qquad (3)$$

EC is very similar to ICG, but has the advantage of providing for the investigation of the hemodynamic properties in patients with low level *COs*, using just two pairs of measuring electrodes instead of four (Fig. 3).

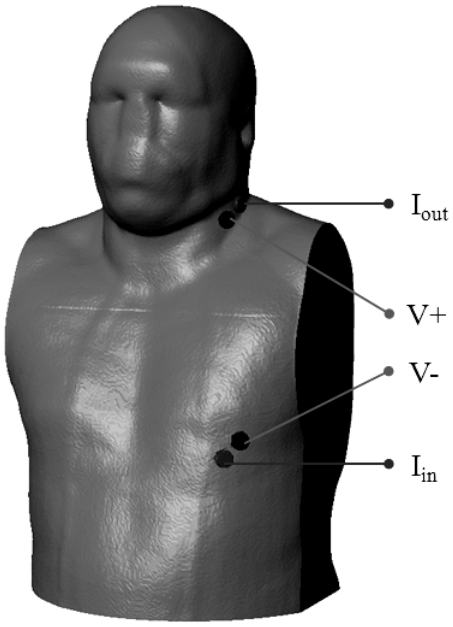

Fig. 3. Electrode setup in the EC technique.

III. THE COMPUTATIONAL DOMAIN

When numerical simulation is used to investigate the outlining features of ICG and EC, the usage of realistic geometries may avoid some of the errors introduced by simplifying idealizations of the computational domains.

In this study we built a patient related image-based 3D computational model and used it to solve for the ICG problem by using the finite element method (FEM). A dataset of 400 *Digital Imaging and Communication in Medicine* (DICOM) high-resolution slices acquired from a healthy subject using a modern Computed

Tomography (CT) scanner [8] is the image data source used in building the 3D computational domain used for numerical simulations.

Using a threshold filter [9], the regions of interest (ROI) were segmented out of the image dataset source, covering only the tissues that needed to be singled out while discarding the rest.

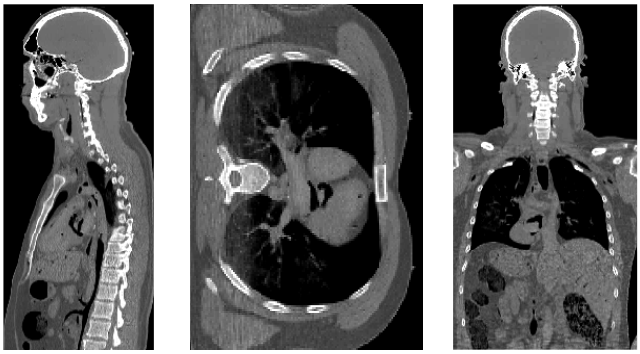

(a) (b) (c)

Fig. 4. High resolution CT images from (a) sagittal, (b) horizontal and (c) transversal workplanes [4].

The result consisted of gross 3D masks of the segmented ROIs. The 3D models were then adjusted using gaussian smoothing and binarisation filters, morphological close, erode, cavity fill and floodfill tools [9], which provided for the spatial continuity of the masks. Spurious artifacts were removed by the bilateral and gradient anisotropic diffusion noise filters [9].

Fig. 5. Regions of interest segmentation [4].

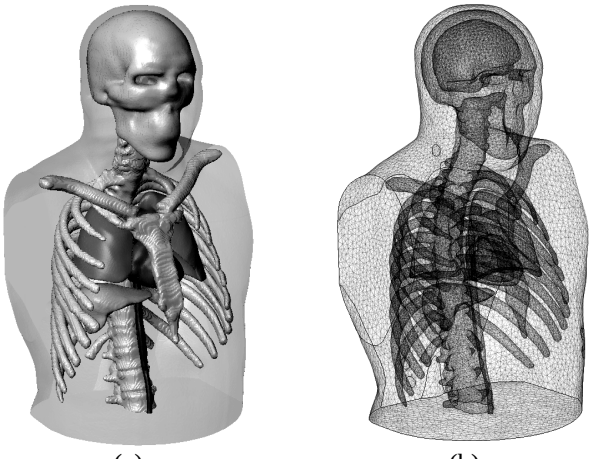

(a) (b)

Fig. 6. The final 3D solid model (a) and the FEM mesh (b).

To differentiate between the internal organs and the thorax tissues and head, several subtraction, inversion, and intersection boolean operations were applied to the segmented masks (Fig. 5). The conductor volume (Fig. 6a) is made of skull, brain, ribs and spinal cord, *myocardium*, blood inside the atriums and ventricles, lungs, liver and the thorax. This is the computational domain in the ICG and EC used for numerical simulations.

Next, the FEM mesh (*approx.* 565,000 Lagrange tetrahedral, quadratic elements) is produced (Fig. 6b).

IV. THE MATHEMATICAL MODEL

ICG and EC models analyses rely on solving an electrical field problem, governed by the

the electrical charge conservation law

$$\nabla \cdot \mathbf{J} = 0\,, \tag{4}$$

the electrical conduction law

$$\mathbf{J} = \sigma \mathbf{E}\,, \tag{5}$$

the consequence to the electromagnetic induction law

$$\mathbf{E} = -\nabla V\,, \tag{6}$$

where $\mathbf{J}$ [A/m^2] is the electrical current density, σ [S/m] is the electrical conductivity, $\mathbf{E}$ [V/m] is the electric field strength, and V [V] is the electrical potential.

The physical model (4)-(6) yield the following mathematical model

$$\Delta V = 0 \tag{7}$$

The boundary conditions (BCs) that close the model are: no current inflow / outflow through the thorax surface ($\mathbf{n}\cdot\mathbf{J} = 0$).

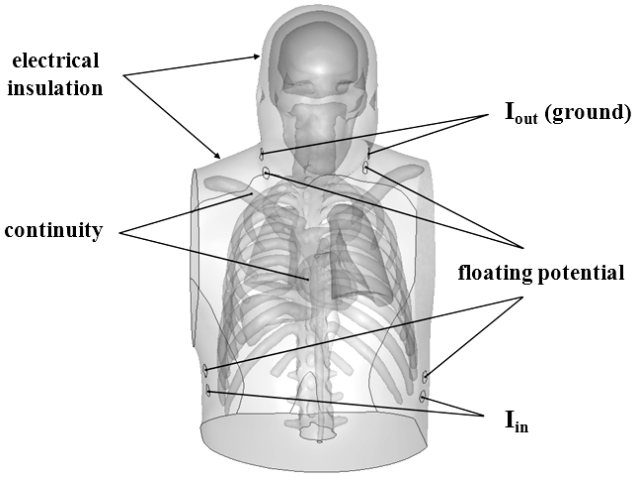

Fig. 7. Boundary conditions in the ICG problem.

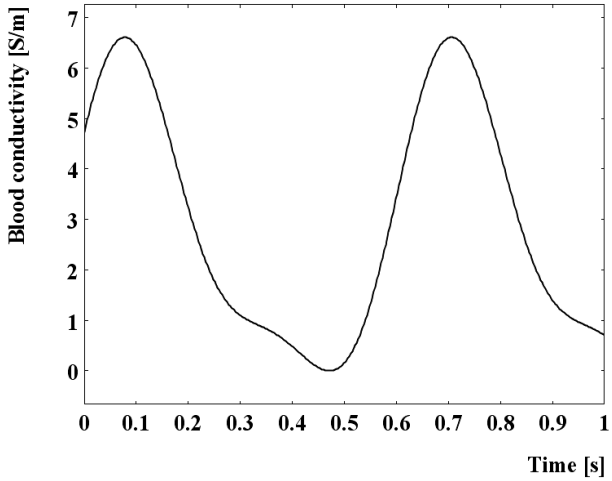

Fig. 8. The time dependent electrical conductivity of blood.

In accordance to the ICG and EC techniques, an 100 μA (rms) electrical current is injected through the bottom electrodes in the abdominal region, while the electrodes placed in the neck region, set as ground, close the electrical current circuit.

The pair of measuring electrodes placed in the middle is set as floating potential spots. Due attention is needed when building the computational domain: a large enough thorax should be generated, considering that its bottom section is assumed electrically insulated. Fig. 7 shows the BCs for the ICG problem. Similar BCs were assumed for the EC problem (Fig. 3).

To simulate the change in electrical conductivity of the aortic segment due to the pulsatile aortic blood flow, we defined a time dependent expression for the electrical conductivity of blood that mimics the blood filling and draining of the vessel and heart chambers domains

$$\sigma(t) = [\mathrm{a}\sin(10t) + \mathrm{b}] \cdot [\mathrm{a}\sin(10t - \varphi) - \mathrm{c}], \quad (8)$$

where *a* is a the parameter used to adjust the sine wave amplitude, *b* sets its delay, *c* controls the cosine waveform amplitude, and φ is the cosine phase shift.

The mathematical model of the electrical field problem described by relation (7) was solved for using the finite element method (FEM) via the GMRES time dependent solver [10].

V. NUMERICAL SIMULATION RESULTS

The electrodes were positioned for the ICG (Fig. 2) and EC (Fig. 3) procedures in the 3D solid model (Fig. 6a).

Once the electrical field problem was solved for, the numerical simulation results highlight the electrical current density distribution in the thorax. For the ICG technique, the electrical current density flux tubes are concentrated mainly in the aortic flow domain (Fig. 9) due to the high electrical conductivity values of the blood.

In the second problem (EC), the electrical current density flux tubes are conveyed, mainly, by the blood flow through the heart chambers.

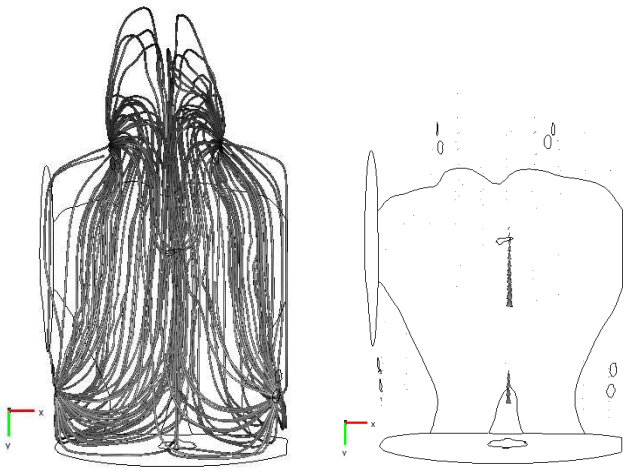

(a) (b)

Fig. 9. The electrical current density distribution in the thorax outlined by (a) flux tubes, and (b) proportional arrows, for maximum blood electrical conductivity (t = 0.705 s) for the ICG procedure.

The waveform of the time dependent thoracic impedance (Fig. 11) for the ICG procedure was generated after calculating the ratio between the measured voltage using the four blue middle potential electrodes (Fig. 2) and the injected 100 μA electrical current.

(a) (b)

Fig. 10. The electrical current density distribution in the thorax by (a) flux tubes, and (b) proportional arrows, for maximum blood electrical conductivity (t = 0.705 s) for the EC procedure.

Fig. 11 shows $Z(t)$ and dZ/dt obtained out of numerical simulation. These results bear the absence of an electrode-skin contact resistance in the model, the limited number of evaluation points considered for the bioimpedance calculation, and electrical conductivity time variation (8) that neglects the phase shift between the pulse waveform and the electrical conductivity. A more realistic approach would aim at coupling the electrical field problem with the blood flow problem in the aorta, to provide for more realistic flow conditions.

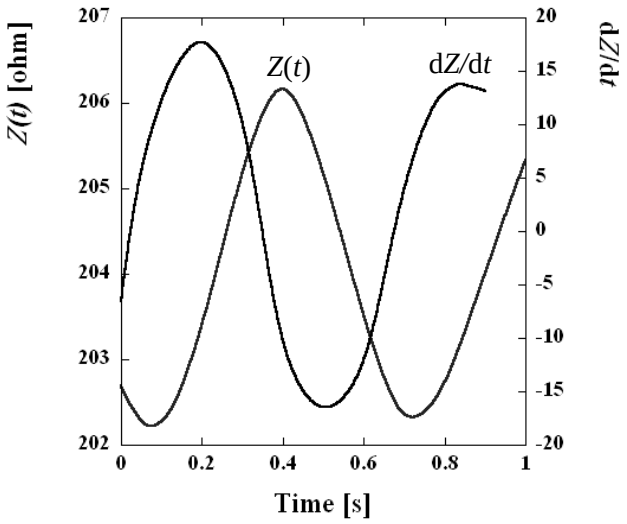

Fig. 11. The time dependent impedance and its derivative.

VI. EXPERIMENTAL RESULTS

Experimental investigations were also conducted on a set of twelve subjects, made of both healthy and heart disease diagnosed people. These experiments refer to the ICG. The position of electrodes is shown in Fig. 2, and the measurements were performed in a quiet atmosphere. The recording and the numerical processing of the physiological signals were conducted with the Biopac MP 150 system and the Acqknowledge software [11] (Fig. 12).

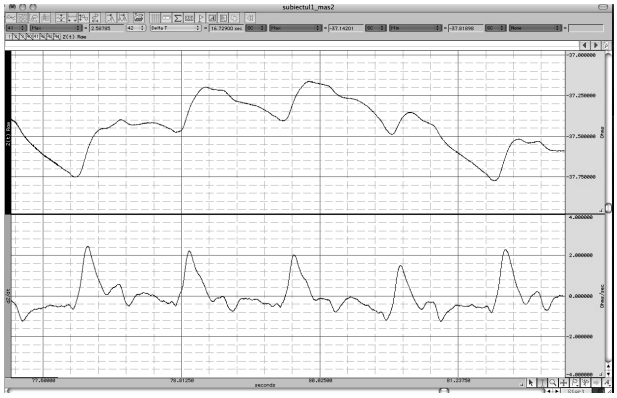

Fig. 12. Recorded and computed signals – the impedance $Z(t)$ (above) and its time derivative dZ/dt (below).

Twelve subjects, aged between 24 and 60, were investigated. They were divided into two groups: 5 of them with different diagnosed cardiac diseases, under continuous medication, and the other 7 in normal health conditions. Table I lists the results obtained from eight subjects. The stroke volume was calculated as presented in equation (2) and the cardiac output (CO) was determined using the following expression

$$CO = SV \cdot HR, \tag{9}$$

where HR represents heart rate [bpm].

TABLE I. *LVET*, *SV* and *CO* values [4].

Subject	*LVET* [s]	*SV* [ml/beat]	*CO* [l/min]
1	0.291	57.039	3.760
2	0.285	44.778	3.330
3	0.294	73.266	5.272
4	0.279	86.927	5.393
5	0.288	64.910	5.270
6	0.313	91.508	5.582
7	0.282	69.753	5.072
8	0.265	50.716	3.984

The statistics presented in Table II validate our experimental data. Also, great similarities between the experimental $Z(t)$ and dZ/dt waveforms (Fig. 12) and the ICG waveforms

from literature (Fig. 1) can be noticed.

TABLE II. Cardiac output related statistics [1], [11].

Parameter	Value
Base thoracic impedance, Z_0 [Ω]	Males: 20–30 Females: 25–30
Change in impedance, dZ/dt [Ω/s]	0.8 – 2.5
Left-ventricular ejection time, T [s]	0.25 – 0.35
Stroke volume, *SV* [ml/beat]	60 –100
Cardiac output, *CO* [l/min]	4 – 8
Cardiac index, *CI* [l/min/m^2] (indexed to body surface area)	2.5 – 4.5

VII. CONCLUSIONS

Numerical simulations of the ICG and EC procedures were conducted on a realistic, CT image based computational domain.

The impedance dynamics, due to the alternate filling and draining of the heart chambers and aorta with blood, was simulated by a time dependent expression for the electrical conductivity.

The numerical simulation results highlight the main differences between the two investigation methods: the ICG evaluation of the thoracic bioimpedance is based on the aortic blood flow, while the EC gives a more heart chamber blood flow related impedance waveform. EC is more accurate when evaluating low value CO patients, like children and neonates.

The discrepancies between the experimental (Fig. 12) and the numerical (Fig. 11) $Z(t)$ and dZ/dt are explained by the absence of an electrode-skin contact resistance in the model, the limited number of evaluation points considered for the bioimpedance calculation, and electrical conductivity time variation (8) that neglects the phase shift between the pulse waveform and the electrical conductivity. A more realistic approach would aim at coupling the electrical field problem with the blood flow problem in the aorta, to provide for more realistic flow conditions. The ICG and EC models will be further developed to simulate more realistic pulsatile flow conditions.

Tables I, II show off small differences between the results – they are within limits, with few exceptions. The persons with various heart diseases present small values for *SV* and *CO*.

The non-invasive hemodynamic monitoring (*e.g.*, stroke volume, cardiac output) decrease costs because of the reduced expenditures for equipment and saves the physicians and nurses time. The information collected from this kind of monitoring process decreases the potentially life-threatening complications of infection and artery perforation.

VIII. APPENDIX

TABLE III. ICG and EC parameters [1], [3], [11], [12].

Parameter	Symbol	Definition
Heart Rate	*HR*	Number of heart beats per minute
Cardiac Output	*CO*	Amount of blood pumped by the left ventricle per minute
Cardiac Index	*CI*	Cardiac output normalized for body surface area
Stroke Volume	*SV*	Amount of blood pumped by the left ventricle each heartbeat
Stroke Index	*SI*	Stroke volume normalized for body surface area
Systemic Vascular Resistance	*SVR*	The resistance to the flow of blood in the vasculature (often referred to as "Afterload")
Systemic Vascular Resistance Index	*SVRI*	Systemic vascular resistance normalized for body surface area
Acceleration Index	*ACI*	Peak acceleration of blood flow in the aorta
Velocity Index	*VI*	Peak velocity of blood flow in the aorta
Thoracic Fluid Content	*TFC*	The electrical conductivity of the chest cavity, which is primarily determined by the intravascular, intra-alveolar, and interstitial fluids in the thorax
Left Cardiac Work	*LCW*	An indicator of the amount of work the left ventricle must perform to pump blood each minute
Left Cardiac Work Index	*LCWI*	Left cardiac work normalized for body surface area
Systolic Time Ratio	*STR*	The ratio of the electrical and mechanical systole
Pre Ejection Period	*PEP*	The time interval from the beginning of electrical stimulation of the ventricles to the opening of the aortic valve (electrical systole)
Left Ventricular Ejection Time	*LVET*	The time interval from the opening to the closing of the aortic valve (mechanical systole)

IX. ACKNOWLEDGMENTS

The work was conducted in the Laboratory for Electrical Engineering in Medicine (IEM), at UPB – a member of the BIOINGTEH platform. A.A. Dobre acknowledges the support offered by the POSDRU/88/1.5/S/61178 grant. M.C. Ipate acknowledges the support offered by the POSDRU/6/1.5/S/19/7713 grant. A.M. Morega acknowledges the research grant CNCSIS PCCE-55/2008.

X. References

[1] Sherwood A., Allen M.T. et al., "Committee Report: Methodological Guidelines for Impedance Cardiography", Psychophysiology, 27, 1, 1990, U.S.A.

[2] Pickett B.P., Buell J.C., "Validity of Cardiac Output Measurement by Computer-Averaged Impedance Cardiography, and Comparison with Simultaneous Thermodilution Determinations", The American Journal of Cardiology, 69, May 15, 1992, pp. 1354-1358.

[3] http://en.wikipedia.org/wiki/Impedance_cardiography.

[4] Ipate M.C., Dobre A.A., Morega A.M., "The Stroke Volume and the Cardiac Output by the Impedance Cardiography", UPB Scientific Bulletin, ISSN 1454-2331.

[5] Albert N.M., Hail M.D et al., "Equivalence of the Bioimpedance and Thermodilution Methods in Measuring Cardiac Output in Hospitalized Patients with Advanced, Decompensated Chronic Heart Failure", AJCC, the American Journal of Critical Care, 2004, 13, pp. 469-479.

[6] Kamath S.A., Drazner M.H. et al., "Correlation of Impedance Cardiography with Invasive Hemodynamic Measurements in Patients with Advanced Heart Failure: the Bioimpedance CardioGraphy (BIG) Sub study of the ESCAPE Trial", Am. Heart J., 2009 August, 158, 2, pp. 217-223.

[7] Van De Water J.M., Miller T.W., "Impedance Cardiography: The next Vital Sign Technology?" Official publication of the American College of Chest Physicians, Chest 2003, 123, pp. 2028-2033.

[8] http://pubimage.hcuge.ch:8080/.

[9] Simpleware v.3.2, Simpleware Ltd., UK, 2010.

[10] Comsol Multiphysics v3.5a, Comsol AB, Sweden, 2009.

[11] http://www.biopac.com/Manuals/app_pdf/app196.pdf

[12] http://www.carestreammedical.com/uploads/file/CASMED-Lifegard_ICG_Rev00.pdf.

XI. Biographies

Alin A. Dobre (IEEE EMB Stud. M.'2009) was born in Ploiesti, Romania, in 1985. He received the B.E. and M.S. degrees in electrical engineering, in 2009, from the Faculty of Electrical Engineering at University POLITEHNICA of Bucharest (UPB), and has a M.S in Medical and Clinical Engineering from the Faculty of Medical Engineering, UPB. He is currently a doctoral student at the Faculty of Electrical Engineering, UPB. His concerns are image-based reconstruction of human tissue, numerical modeling and simulation of physiological processes and clinical procedures.

Mihaela C. Ipate (IEEE EMB Stud. M'2010) was born in Calarasi, Romania, in 1984. She received B.E. and M.S. degrees in electrical engineering, in 2008, a M.S. degree in electrical sensors, 2010, and the Dr. degree in electrical engineering, 2011, from the Faculty of Electrical Engineering at University POLITEHNICA of Bucharest (UPB). Her research interests are electrical signals acquisition and data processing in medical engineering, numerical modeling and simulation s.

Alexandru M. Morega (IEEE EMB, IAS SM'2007) was born in Bucharest, Romania, in 1955. He received the B.E. and M.S. degrees in electrical engineering from the University POLITEHNICA of Bucharest, Bucharest, Romania, in 1980, the Dr. degree in electrical engineering from the University POLITEHNICA of Bucharest, in 1987, and the Ph.D. degree in mechanical engineering from Duke University of Durham, North Carolina, USA, in 1993. He is Professor at the Faculty of Electrical Engineering, University POLITEHNICA of Bucharest. His current research interests include electromagnetism, heat and mass transfer, field-substance interactions, energy conversion and sources, multiphysics modeling. Prof. A. M. Morega is a senior researcher of "Gh. Mihoc – C. Iacob" Institute of Applied Mathematics, Bucharest, at the Romanian Academy. He is Member (1990) of the American Society of Mechanical Engineers (ASME), and Chair of the Romanian Chapter of the Engineering in Medicine and Biology Society, IEEE (IEEE-EMBS). http://www.iem.pub.ro/~amm

Electromechanical Transduction Effects in Dielectric Elastomers

*Alexandru-Laurentiu Catanescu, **Ioan Puflea
Research and Development National Institute of Electrical Engineering (INCDIE ICPE-CA),
Splaiul Unirii, No. 313, District 3, 030138, Bucharest, Romania, *catanescu@icpe-ca.ro,

Abstract – Dielectric elastomers are electromechanical transducers that convert electrical energy to or from mechanical energy. In an actuator mode, dielectric elastomers convert electrical to mechanical energy, where as in a generator mode they perform the reverse function and convert mechanical to electrical energy.

This paper derives the fundamental equations describing dielectric elastomer transduction. The equations show quantitatively how electrical parameters such as electric field and dielectric constant are related to mechanical parameters such as stress and strain.

***Index Terms* – dielectric elastomers (DE), electromechanical transducers, actuators, variable stiffness, stability.**

I. Introduction

Dielectric elastomers (DE) are electromechanical transducers that convert electrical energy to mechanical energy. Transducers that convert electrical to mechaical energy are actuators. DE can also convert in the reverse direction; in this type of operation, DE are acting in a generator mode. In this paper, the focus will be on the fundamental aspects of DE as transducers.

II. Fundamentals of DE Transduction

The basic structure of DE, shown in fig. 1 [1], is quite simple. A polymer film, typically an elastomer, is sandwiched between two electrodes. The electrodes in a DE transducer are compliant, with the level of compliance determined by the specifics of the DE transducer such as the magnitude of strain that must be accommodated.

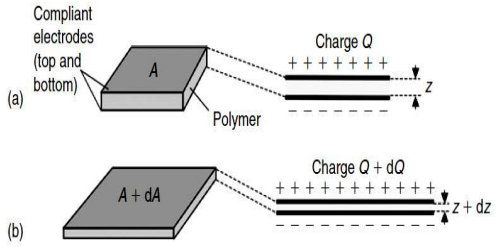

Fig. 1. Charged DE film (a) in an initial stage and
(b) in an incrementally changed final state. Changes exaggerated for clarity.

The behaviour of DE can be derived in a number of ways. Methods involving tensors are the most general and several analysis using tensors have been developed [2÷6]. But the generality of tensor approaches can obscure the simplicity of the underlying physics. Here an energy approach will be used to develop the important equations for DE.

The DE film, including electrodes, is an electrically capacitor (capacitance C). The electrical energy of the capacitor W_e with charge Q can be written as

$$W_e = \frac{1}{2}\frac{Q^2}{C}, C = \frac{\varepsilon_0 \varepsilon_r A}{2}, W_e = \frac{Q^2 z}{2\varepsilon_0 \varepsilon_r A} \quad (1)$$

with the assumptions:

$$W_e = W_e(Q, z, A), \varepsilon_r = ct, Vol = Az = ct \quad (2)$$

Using eq. (1) and (2), the change in electrical energy dW_e is written as

$$dW_e = VdQ + 2W_e \frac{dz}{z} = VdQ - 2W_e \frac{dA}{A} \quad (3)$$

where $\delta L_e = VdQ$ is the electrical energy from an external source and $\delta L_i = -2W_e dz / z = 2W_e dA / A$ is the work done by the electric field.

Equation (3) are useful for understanding the two important modes of DE:

$$\begin{cases} dz < 0 \Rightarrow dW_e \downarrow \Rightarrow DEactuator; \\ dz > 0 \Rightarrow dW_e \uparrow \Rightarrow DEgenerator \\ dA > 0 \Rightarrow dW_e \downarrow \Rightarrow DEactuator; \\ dA < 0 \Rightarrow dW_e \uparrow \Rightarrow DEgenerator \end{cases} \quad (4)$$

The resultant Maxwell stress, sometimes called effective pressure or actuation pressure, can be defined by the equation

$$\delta L_i = -Apdz \quad (5)$$

Equation (3) and (5) lead to

$$p = -\frac{1}{A}(\frac{\delta L_i}{dz})_{Q=ct} = \frac{1}{A}(\frac{dW_e}{dz})_{Q=ct} = \frac{2W_e}{Az} = 2w_e = \varepsilon_0 \varepsilon_r E^2 \quad (6)$$

The resultant Maxwell stress in equation (6) is twice the coresponding normal stress per unit area in a parallel plate capacitor device. The additional factor of 2 is because DE have a second coupled degree of freedom to convert electrical to mechanical energy compared with air-gap parallel plates. The two modes of conversition can be treated separately (compressive stress in the z-direction and tensile stresses in the planar direction), but since the two modes are coupled via the constant volume condition in an elastomer, it's more convenient to speak of a single effective pressure or resultant Maxwell stress rather than two separate components.

III. Stiffness model

It's analyzed a stiffness model using the basic trasduction mechanism of DE. Let W_m be the elastic mechanical energy stored in the material:

$$W_m = k_0 \frac{(z - z_0)^2}{2} \quad (7)$$

where k_0 is the mechanical stiffness with zero charge and z_0 is taken as relaxed thichness of the film.

If the material is stretched an amount dz in thickness by an external force F applied adiabatically in the z-direction, an amount of external work Fdz is done on the DE. The energy balance of the system is used to find F:

$$Fdz = dW_m + dW_e - VdQ \quad (8)$$

Taking in account that

$$dW_e - VdQ = 2W_e \frac{dz}{z} \quad (9)$$

F can be written as

$$F = k_0(z - z_0) + \frac{2W_e}{z} \quad (10)$$

The stiffness of the system can now be found using equation

$$k = \frac{dF}{dz} \quad (11)$$

A constant charge electrical loading gives

$$dQ = 0 \Rightarrow W_e = \frac{Q^2 z^2}{2\varepsilon_0 \varepsilon_r Vol}, F = k_0(z - z_0) + \frac{Q^2 z}{\varepsilon_0 \varepsilon_r Vol}, k = k_0 + \frac{Q^2}{\varepsilon_0 \varepsilon_r Vol} \quad (12)$$

and a constant voltage electrical loading gives:

$$dV = 0 \Rightarrow W_e = \frac{\varepsilon_0 \varepsilon_r V^2 Vol}{2z^2}, F = k_0(z - z_0) + \\ + \frac{\varepsilon_0 \varepsilon_r Vol}{z^3}, k = k_0 - \frac{\varepsilon_0 \varepsilon_r V^2 Vol}{z^3} \quad (13)$$

This are illustrated in fig. 2, [7], which shows a qualitative graph of the external force F needed to achieve a given contraction of z.

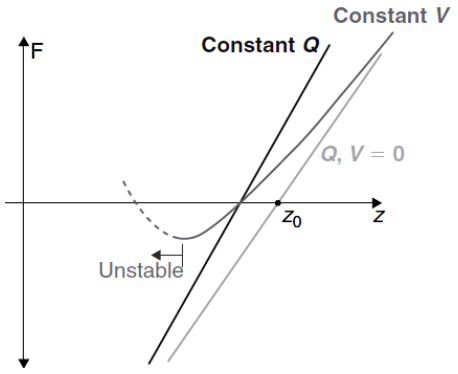

Fig. 2. D E thickness versus applied force under different electrical conditions.

Note that if the second therm on the right hand side of equation (13) gets sufficiently negative, the stiffness goes to zero and becomes negative for decreasing z:

$$z \le z_0 = \sqrt[3]{\varepsilon_0 \varepsilon_r V^2 Vol / k_0} \Rightarrow k \le 0 \quad (14)$$

A negative stiffness implies DE is unstable and this regime must tipically be avoided in a DE.

IV. Modeling DE actuation

On starts with equation (6) in the form

$$p = -\varepsilon_0 \varepsilon_r E^2 = -\varepsilon_0 \varepsilon_r \frac{V^2}{z^2} \quad (15)$$

and using Hooke's low [4]

$$p = Y(z - z_0)/z_0 \quad (16)$$

where Y is the elastic modulus on obtains algebric equation

$$(\frac{z}{z_0})^3 - (\frac{z}{z_0})^2 + \frac{\varepsilon_0 \varepsilon_r V^2}{Y z_0^2} = 0 \quad (17)$$

With the substitution $z / z_0 = u / 3$, results canonical form of equation $u^3 + pu + q = 0$ which is solved by Ghermanescu's method: $u = t - p/3$. Finally, using a lot of fancy algebra on finds a formula for the height as a function of the applied voltage:

$$\frac{z}{z_0} = \frac{1}{3}(1 + f_0 + \frac{1}{f_0}) \quad (18)$$

where

$$C = \frac{\varepsilon_0 \varepsilon_r V^2}{Y z_0^2}, f_0 = [1 - 13,5C + \\ 0,5(81C^2 - 12C)^{1/2}]^{1/3} \quad (19)$$

Using these formulas on can see how elastomer VHB4910 with $z_0 = 0,1mm, Y = 3MPa, \varepsilon_r = 5$, [6], will compress when a voltage is applied across it – fig. 3.

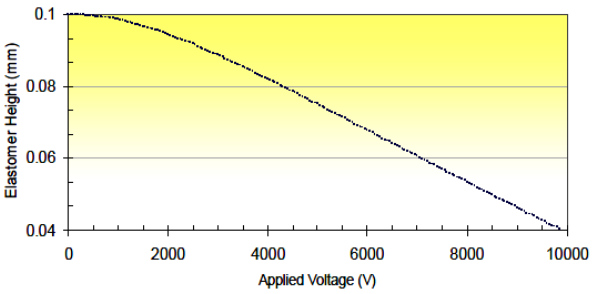

Fig. 3. Compressive Vertical Strain vs. Applied Voltage.

V. Conclusions

The basic energy relation of DE transduction have been described. If an electric charge or voltage is on the DE film that is expanding in area, the film is converting electrical to mechanical energy

and operating in an actuator mode. If a charged film is contracting in area energy is being converted from mechanical energy to electrical energy and the film is operating in a generator mode.

A key simplification in the energy equations can be achieved for true elastomers and other soft polymers where volume can be assumed constant.

These equations can be used to analyse a number of important conditions for DE, such as constant charge or constant voltage condition, stability as a function of strain, models for stiffness and actuation. The equations developed may give a better understanding of detailed applications.

VI. Acknowledgment

This work has been supported by the financial support of the nucleus ANCS Romanian authority project no.PN 09-35-01.01/2009.

VII. References

[1] Carpi F., "Dielectric Elastomers as Electromechanical Transducers", Oxford UK, Elsevier 2008, pp. 3.

[2] Khedimi F., "Modelisation micromecanique des elastomères chargés", Thèse de doctorat, Aix-Marseille Université, 2011.

[3] Wissler M.T., "Modeling Dielectric Elastomer Actuators", PhD Thesis, Federal Institute of Technology, Zurich, 2007.

[4] Kofod G., "Dielectric Elastomer Actuators", PhD Thesis, Technical University of Denmark, 2001.

[5] Pelrine R., "High-fied deformation of elastomeric dielectrics for actuators", Materials Science and Engineering C 2000, Vol. 11, pp. 89, 2008.

[6] Plante J.S., "On the proporties of dielectric elastomer actuators and their design implications", Smart Materials and Structures, Vol. 16, No. 2, 2009.

[7] Choi H., "Electroactive Polymer Actuators and Devices", Smart Materials and Structures, Vol. 4695, pp. 138, 2002.

VIII. Biographies

Catanescu Alexandru-Laurentiu was born in Slatina, Romania, on March 22, 1983. He graduated from the Faculty of Electrical Engineering, Polytechnic University in Bucharest on 2007, and received a Masters Degree Diploma from the same Faculty in 2009. Nowadays I'm Phd student of Bucharest Polytehnic University, faculty of Electrical Engineering.

His employment experience includes the National Institute for Research and Development in Electrical Engineering ICPE-CA, Department of Electro-mechanical Engineering.

His fields of interest include electrical machines, electromagnetic, piezoelectric and magnetostrictive actuators.

Puflea Ioan was born in Sighisoara, Romania, on April 25, 1948.He graduated from Bucharest Polytehnic University at 1971 and he received Ph.D. degrees in electrical engineering from Bucharest Polytehnic University in 1980.

His employment experience included the National Research Electrical Engineering Institute, Dep. of Electromechanical Engineering. The research preoccupation are electromagnetic field computation, superconducting windings design, electric machines and apparatus design.

Interferometric Microscope Investigation Method. Results and Capabilities

*Dragos Ovezea
Research and Development National Institute of Electrical Engineering (INCDIE ICPE-CA), Splaiul Unirii, No. 313, District 3, 030138, Bucharest, Romania, *dragos.ovezea@icpe-ca.ro

Abstract – The paper presents the results of several measurements on different samples, made with the Wyko NT 1100 interferometric microscope (profilometer) and a comparison with the results obtained with a different microscope. The tests were conducted in the LMNEM (Laboratory for Measurments on Micro and Nano Mechanics).

***Index Terms* – profilometer, interference, Mirau, FR4, interdigital electrodes.**

I. Introduction

This paper presents the results of measurements on several samples of material on Wyko NT1100 interferometric microscope. The microscope has a Mirau interferometer and uses an optical scanning method called Vertical Scanning Interferometry (VSI), [1]. The microscope has yet another measurement method called Phase Shift Interferometry (PSI). These two methods allow for a scanning domain of up to 2mm and resolutions less than 0.1nm.

The microscope is used for determining roughness, height, distance, cylindricity, sphericity.

II. Exploration of surfaces through interferometry

The general structure of the interference microscope Wyko NT1100 is shown in fig.1 and is comprised of a white light source (light source, aperture stop, filter, field stop), beam splitter, translator, objective, Mirau interferometer and CCD detector array. The combination of optical components available for the microscope allow for two sizes of the field of vision: 1.3x0.95mm and 255x191µm.

Measurements were made on different types of surfaces and the results are being shown in this paper.

Ni Spurs

On a Si wafer covered in gold was deposited Ni in a mask made of SU8. Being known the height of the SU8, measurements were made in order to determine the distance between SU8 surface and the interior Ni deposition. In figure 2 is shown an image of a spur, as seen by the CCD sensor.

In figure 3 is shown the captured data transformed in height and presented as color map, and in figure 4 a three dimensional representation of the height map of the visible surface.

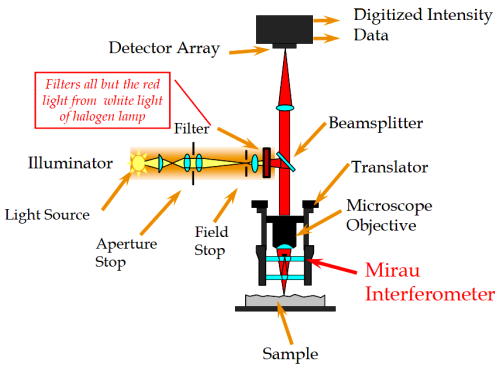

Fig. 1. General structure of the microscope.

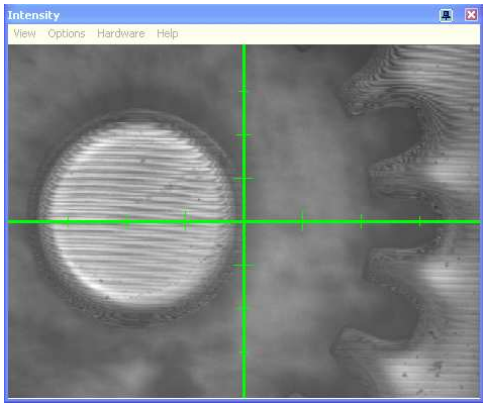

Fig. 2. Image captured from the CCD array.

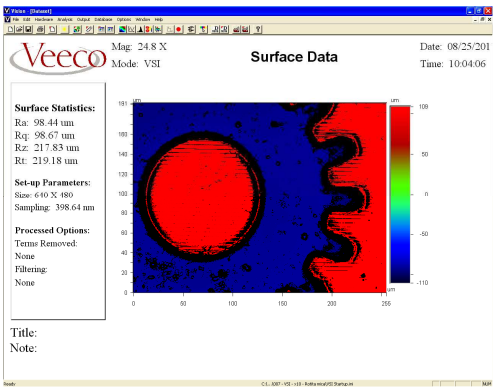

Fig. 3. Height color map of the SU8 mask and Ni in VSI mode.

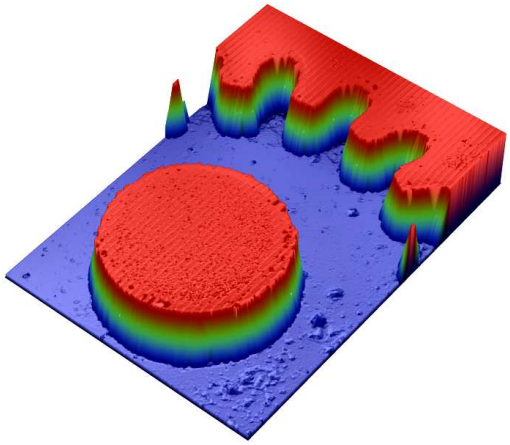

Fig. 4. 3D representation.

Scalpel blade

In figure 5 can be shown the 3D representation of the steel surface of a scalpel. In the image can be seen a portion of the number 2 stamped on its surface for the purpose of identifying the size.

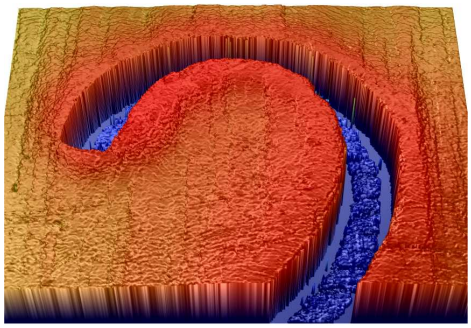

Fig. 5. Scalpel identification number.

Serial number printings on plastic container

The shape of dried ink on a plastic pill container can be seen in figure 6.

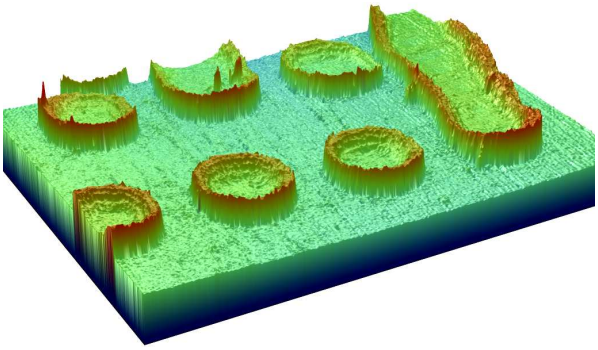

Fig. 6. Ink markings on plastic surface.

Tic-Tac pill surface roughness

In figures 7 and 8 are displayed the results of a roughness measurement on a pill, without and with sphericity correction.

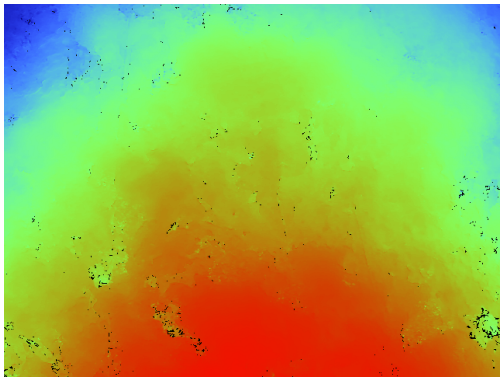

Fig. 7. Pill surface roughness.

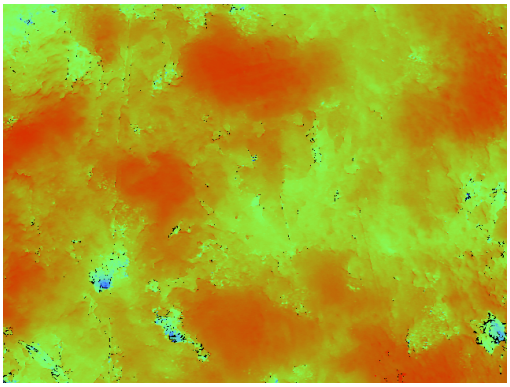

Fig. 8. Pill surface roughness with sphericity compensation.

Paper fibres

Figure 9 shows the surface of a piece of paper with visible individual fibres.

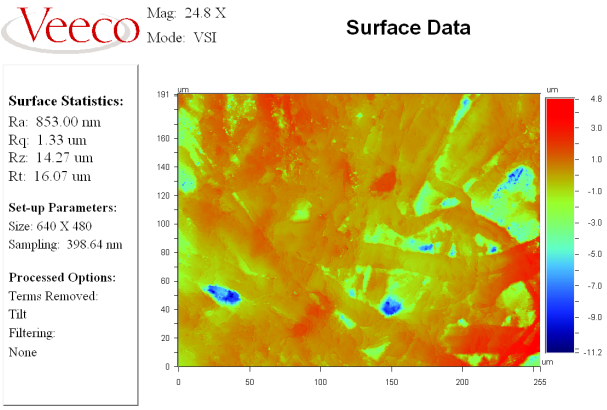

Fig. 9. Paper sheet roughness, visible fibers.

The Wyko microscope allows the export of various results based on the acquired data. The primary way of exporting data is in ASCII files consisting of a header followed by the data. Another data format is CSV, easily loaded in spreadsheet software (figure 10).

	A	B	C	D
1	x	y0		
2				
3	um	um		
4	0	-0.03937		
5	0.398637	0.002022		
6	0.797275	-0.00846		
7	1.19591	-0.05619		
8	1.59455	-0.01629		
9	1.99319	0.056049		
10	2.39182	0.133862		
11	2.79046	0.051619		

Fig. 10. Data saved in CSV format and loaded in a spreadsheet application.

Also, direct height measurements can be seen in figure 11. The data can be averaged and roughness results are calculated from the selected values.

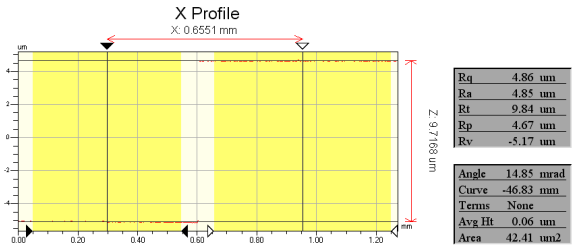

Fig. 11. Height data can be measured along a line.

III. Weaknesses and strengths of the interferometric profilometer

A comparison was made between measurements made on Wyko NT1100 and Semi C200, on a failed grid intended for use in an exploratory research for humidity sensors. The interdigital electrodes were excessively corroded and in some places interrupted. Images of the electrodes taken by Semi C200 can be seen in figures 12 and 13. Images obtained by Wyko microscope are shown in fig 13: black and white interference image to left and color coded height map to right.

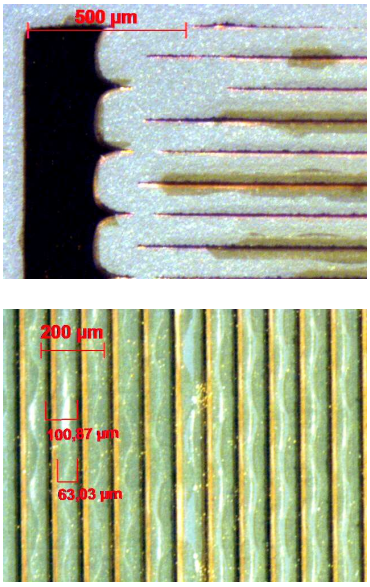

Fig. 12. Electrodes, as seen by Semi C200.

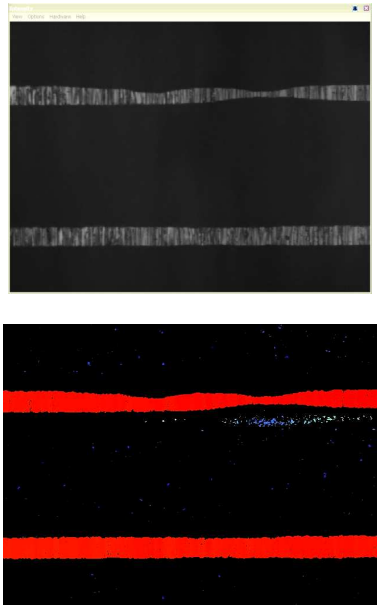

Fig. 13. Electrodes, as seen by WykoNT1100.

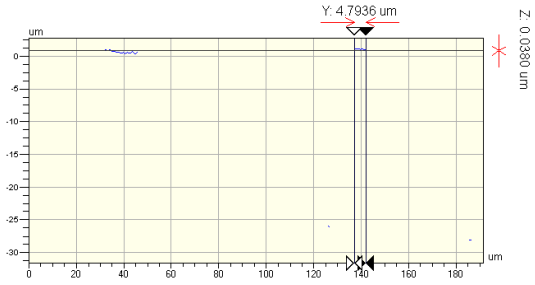

Fig. 14. Measurement of the width of a copper electrode.

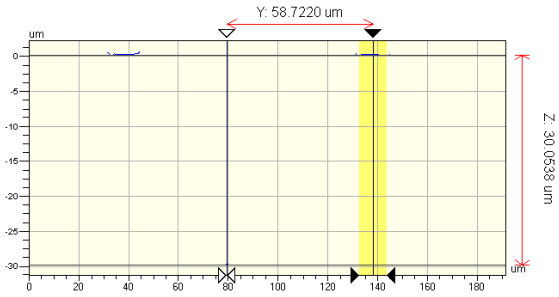

Fig. 15. Measurement of the height of the copper electrode.

Unlike regular optical microscopes, the interferometric method also gives information concerning the height of the structures observed.

The weak point however is the necessity for the surfaces observed to have reflexive surfaces and not to have to steep slopes. If any of the two conditions are not met then no information can be obtained concerning that particular area. In figure 13, these areas are color coded in black (right image). The substrate supporting the copper was FR4 and while is visible under regular microscopes it is not suitable for the interferometric method. While most of the FR4 surface could not be measured, the position of some points could be recorded. Using these points, the height of the copper electrodes was determined (fig 15) to be 30µm. The width at the top of the electrodes was measured at a point where the electrode was visibly more corroded but not interrupted. The width was found to be 5µm (fig 14) so the obtainable electrodes can have a height to width aspect ratio of 6.

As seen in figure 12, the photoresist layer on the top of the electrodes has not been completely dissolved, thus creating an undesired protective shield over much of the area to be corroded.

IV. Conclusions

The Wyko NT1100 profilometer is a versatile instrument giving an ample amount of data about the investigated areas but also has limitations. The best method of investigation for various samples should be chosen accordingly to the type of materials to be observed. While the interferometric method gives accurate results, the access to data is restricted by the necessity to obtain sets of interference fringes in order to calculate distances and thus, the lack of reflectivity can be a problem.

One solution to this problem is increasing the optical magnification of the microscope or the resolution of the CCD camera sensor which allows for discrimination between the reflected light read as pixels intensity.

On the good side, the ability to export numerical data ensures a much better opportunity for measurement as data can be read at a later time and processed.

V. Acknowledgement

The author gratefully acknowledges the support obtained from INCDIE ICPE-CA through the kernel type project 5303/2009 for offering the samples of interdigital electrodes.

VI. References

[1] Wyko surface profilers – User Guide

VII. Biography

Ovezea Dragoş was born in Bucharest on November 26, 1979. He graduated in 2005 and is currently a Ph.D. student in mechatronics at the Politehnica University of Bucharest.

His employment experience include several research and development projects at Politehnica University of Bucharest's Center for Research and Development for Mechatornics (CCDM).

The research preoccupations include piezoelectric and electric actuations, electric circuit and PCB design, CAD.

Inorganic materials for thermoelectric generators. A review.

*Gabriela Telipan
Research and Development National Institute of Electrical Engineering (INCDIE ICPE-CA), Splaiul Unirii, No. 313, District 3, 030138, Bucharest, Romania, gtelipan@icpe-ca.ro

Abstract – Thermoelectric materials which can generate electricity from waste heat can be used in the solid state thermoelectric generators. For the use in this devices is important to identify the materials with higher thermoelectric performance like figure of merit, Seebeck coefficient, electrical and thermal conductivity. Several inorganic thermoelectric materials are discussed from the point of view of the influence of synthesis method and the crystalline structure about the performance of material for use in the thermoelectric generators.

***Index Terms* –electrical conductivity, figure of merit, power factor, Seebeck coefficient, thermal conductivity, thermoelectric generators, thermoelectric materials.**

I. INTRODUCTION

Thermoelectric (TE) materials have great potential for applications in both power generation and solid state cooling or heating, [1].

The TE power generation could be widely used as a special power source and as novel energy harvesting systems such as waste heat recovery and high efficiency solar energy conversion[1]. Thermoelectric systems can be easily designed to operate with small heat sources and small temperature differences. Such small generators could be mass produced for use in automotive waste heat recovery or home co-generation of heat and electricity. Thermoelectrics have even been miniaturized to harvest body heat for powering a wristwatch, [2]. Heat dissipated from the human body in the form of respiration, skin convection, sweat and skin radiation proved the feasibility of using thermoelectric generators. Experimental results further showed that a dense array of Bi_2Te_3 thermopiles can generate 10 µA at 3V with a temperature difference of 5 degrees to drive low drain electronics, [3].

The thermoelectric generators have the advantages such:

- they are extremely reliable (typically exceed 100,000 hours of steady-state operation) and silent in operation since they have no mechanical moving parts and require considerably less maintenance;
- they are simple, compact and safe;
- they have very small size and virtually weightless;
- they are capable of operating at elevated temperatures;
- they are suited for small-scale and remote applications typical of rural power supply, where there is limited or no electricity;
- they are environmentally friendly;
- they are not position-dependent; and they are flexible power sources, [4].

II. THEORY

As the heat flows from hot to cold, free charge carriers (electrons and holes) in the material are driven to the cold end - Fig. 1.

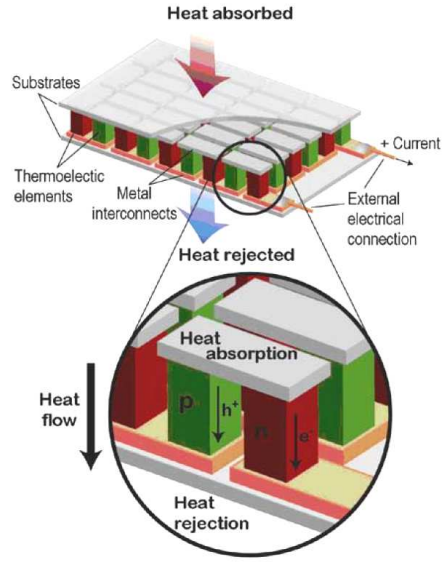

Fig.1. Schematic of a thermoelectric generator.

Many thermoelectric couples (top) of n-type and p-type thermoelectric semiconductors are connected electrically in series and thermally in parallel to make a thermoelectric generator. The flow of heat drives the free electrons (e^-) and holes (h^+) producing electrical power from heat.

The resulting voltage (V) is proportional to the temperature difference (ΔT) via the Seebeck coefficient, α:

$$U = n\alpha\Delta T \tag{1}$$

Where: n is the number of the thermal couple, α is a specific thermoelectric coefficien [4-6].

A thermoelectric generator converts heat (Q) into electrical power (P) with a efficiency η:

$$P = \eta Q \tag{2}$$

The efficiency of a thermoelectric generator depends heavily on the temperature difference $\Delta T = T_h - T_c$ (T_h is the temperature of heat site and T_c is the temperature of cold site) across the device. This is because the thermoelectric generator, like all heat engines, cannot have on efficiency greater than that Carnot cycle:

$$T_h - \frac{T_c}{T_h}$$

The efficiency of a thermoelectric generator is defined as:

$$\eta = \frac{\Delta T}{T_h}\frac{\sqrt{1+ZT}-1}{\sqrt{1+ZT}+\frac{T_c}{T_h}} \tag{3}$$

Where: the first term is the Carnot efficiency and ZT is the figure of merit for the device expressed by

$$ZT = \frac{\alpha^2\sigma T}{k} \tag{4}$$

where: α is the Seebeck coefficient, σ is the electrical conductivity, T is the temperature and k is thermal conductivity.

Fundamental in the field of thermoelectric materials is the need to optimize a variety of conflicting properties. The maximize the thermoelectric figure of merit (ZT) of a material, a large thermopower (absolute value of the Seebeck coefficient), high electrical conductivity and a low thermal conductivity are required.

To ensure that the Seebeck coefficient is large there should only be a single type of carrier. Mixed n-type and p-type conduction will lead to both charge carrier moving to the cold end cancelling out the induced Seebeck voltages. Low carrier concentration insulators and even semiconductors have large Seebeck coefficient in accord with equation, [7,8]:

$$\alpha = \frac{8\pi^2 k_B^{\ 2}}{3eh^2} m^* T\left(\frac{\pi}{3n}\right)^{2/3} \tag{5}$$

where: k_B is Boltzmann's constant, e is the charge of an electron, is Planck's constant, m^* is the effective mass of the carrier, T is temperature, n is the carrier concentration.

However, low carrier concentration also

results in low electrical conductivity:

$$\sigma = ne\mu \quad (6)$$

where: μ is the mobility

The interrelationship between carrier concentration and Seebeck coefficient can be seen from relatively simple models of electron transport. For the metals or degenerative semiconductors, the Seebeck coefficient is characterized by the equation (5).

Fig. 2 shows the compromise between large thermopower and high electrical conductivity in thermoelectric materials that must be struck to maximize the figure of merit. This peak occurs at carrier concentration between 10^{19} -10^{21} carriers per cm^3 (depending on the material system) which falls in between common metals and semiconductors.

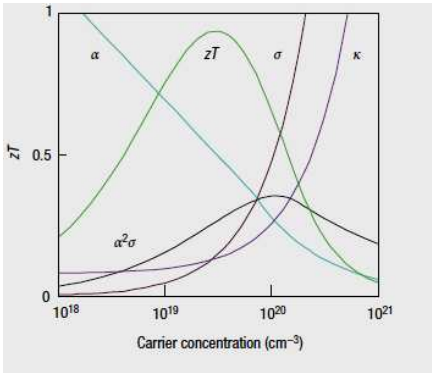

Fig. 2. Optimizing ZT through carrier concentration tuning. Maximizing the effieciency (ZT) of a thermoelectric involves a compromise of thermal conductivity (k plotted on the y axis from 0 to a top value of 10W/mK) and Seebeck coefficient (α:0-500 μV/K) with electrical conductivity σ : 0-5000 $\Omega^{-1}cm^{-1}$.

The effective mass of the charge carrier provides another conflict as large conflict because a large effective masses produce high thermopower but low electrical conductivity. The m^* from eq. 5 refers to the density-of-states effective mass, which increases with flat, narrow bands with high density of states at the Fermi surface, [7]. The relationship between effective mass and mobility is very complex and depends on electronic structure, scattering mechanisms and anisotropy.

A balance must be found between the high effective mass and high mobility. High mobility and low effective mass is typically found in materials made from elements with small electronegativity, whereas high effective masses and low mobilities are found in materials with narrow bands such ionic compounds. A good thermoelectric materials can be found within a wide range of effective masses and mobilities, from low-mobility, high effective mass polaron conductors like oxides, chalcogenides to high mobility, low effective mass semiconductors (SiGe, GaAs).

The thermal conductivity in thermoelectric comes from two sources: electrons and holes transporting heat (k_e) and phonons travelling through the lattice (k_l). Most of the electronic term is directly related to the electrical conductivity through the Wiendemann –Franz law:

$$k = k_e + k_l \quad (7)$$

And

$$k_e = L\sigma T = ne\mu LT \quad (8)$$

where L is the Lorenz factor, $2{,}4x10^{-8}$ $J^2K^{-2}C^{-2}$ for the free electrons.

In addition to optimizing the electronic transport properties, the lattice thermal conductivity must also be low, such as that of an amorphous glass, to achieve high ZT. These criteria have lead to the concept that the ideal material has the electronic structures of a compound semiconductor with the atomic structure of a glass or an “electron-crystal, phonon –glass”.

However, in the absence of precise data on the thermal conductivity, the performance is assessed with the TE power factor (PF) definite by:

$$PF = \alpha\sigma \quad (9)$$

The power factor is used when the materials have similar thermal

conductivities. [9-11].

III. MATERIALS

A good thermoelectric must have a high Seebeck coefficient and electrical conductivity and low thermal conductivity in special a low lattice thermal conductivity. Generally the values of this properties are: Seebeck coefficient 150-230 μV/K, electrical resistivity 1-3 x10^{-3} Ω cm, and thermal conductivity 1,5-3 W/mK [12].

By far the most widely thermoelectric materials are alloys of Bi_2Te_3 and Sb_2Te_3. For near room temperature applications to up to 200°C, Bi_2Te_3 alloys have been proved to possess the greatest figure of merit ZT~1, for both n and p type thermoelectric systems. Alloying Bi_2Te_3 with Sb_2Te_3 was obtained a reduction in lattice thermal conductivity. The most commonly studied p-type compositions are near $Bi_2(Te_{0,8}Sb_{0,2})_3$ type n and $(Sb_{0,8}Bi_{0,2})Te_3$ type p.

The values of figure-of merit for this materials are typically in the range of 0.8 to 1.1-Fig. 3 a.,b., and the Carnot efficiency is 10% [7, 11, 13, 14].

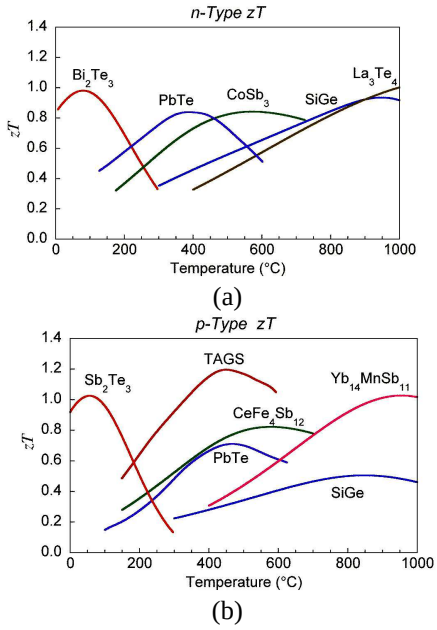

Fig.3 Figure of merit ZT of commercial materials developed by NASA for thermoelectric power generation. a) *zT* for n-type thermoelectric materials, b) *zT* for p-type thermoelectric materials.

For middle temperature power generation 500-900K, materials based on group IV are typically used such PbTe, GeTe or Sn-Te.The ZT value is about 0.8. Alloys, particularly with $AgSbTe_3$, have led to several reports of ZT>1 for both n-type and p-type materials. Only the type $(GeTe)_{0,85}(AgSbTe_2)_{0,15}$ named TAGS with a maximum ZT greater than 1.2, has been used in long life thermoelectric generators. For high temperature >900K thermoelectric generators have typically used silicon-germanium alloys for both n-and p-type legs. The ZT of these materials is fairly low, particularly for the p-type material Fig. 3b., because of the relatively high lattice thermal conductivity of the diamond structure, [7].

One common feature of the thermoelectric recently discovered with ZT>1 is that must have lattice thermal conductivity that are lower than the present commercial materials. These are three general strategies to reduce lattice thermal conductivity:

- The scatter phonons within the unit cell by creating rattling structures or point defects such as interstitials vacancies or by alloying;
- The use complex crystal structures to separate the electron-crystal from the phonon-glass, the goal is to be able to achieve a phonon glass without disrupting the crystallinity of the electron transport region;
- Scatter phonons at interfaces, leading to the use of multiphase composites mixed on the nanometer scale, [7].

The potential to reduce thermal conductivity through disorder within the unit cell is particularly large in structures containing void spaces. One class of such materials are clathrates, which contain large cages that are filled with rattling atoms. Likewise, skutterudites such $CoSb_3$ contain

a unit cell composed by 8 cubes corner sharing $CoSb_3$ octahedra which can be viewed as a distorted variant of the RuO_3 structure. These titled octahedra create void spaces that may be filled with rattling atoms, as shown in Fig. 4 with a blue polyhedron. This binary skutterudite present a Seebeck coefficient of 630 μV/K and a ZT between 0.8-1.1 for the 1200°C, but the thermal conductivity is relative high.

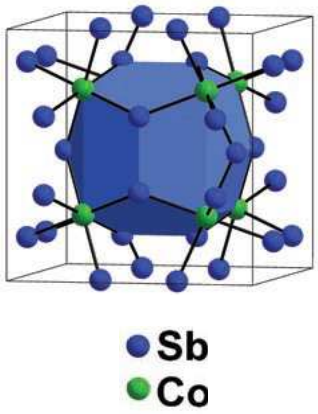

Fig. 4. The skutterudite structure composed by octahedral $CoSb_3$creating large voidsspaces shown in blue.

Filling the large void spaces with rare-earth or other heavy atoms further reduces the lattice thermal conductivity. A good example is the compound $CeFe_4P_{12}$ which present a thermal conductivity 1W/mK [7, 15,16].

Low thermal conductivity is generally associated with crystals containing large complex unit cell. An exeample are the compounds Ag_9TlTe_5 and Tl_9BiTe_6. Although these materials do have complex unit cells, there is something unique about thallium chemistry that leads to low thermal conductivity 0,23 W/mK at room temperature [7]. The zintl compound Zn_4Sb_3 possesse a high ZT >1, which arise from the low glass-like thermal conductivity. In the room temperature phase about 20% of the Zn atoms are on three crystallographically distinct interstitial sites as shown in Fig. 5.

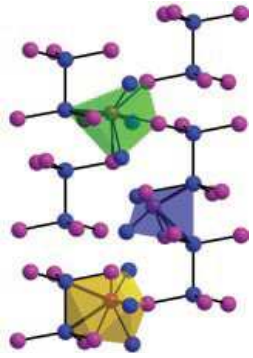

Fig. 5. The room-temperature structure of Zn4Sb3 has a crystalline Sb sublattice (blue) and highly disordered Zn sublattice containing a variety of interstitial sites (in polyhedra) along with the primary sites (purple)

This complex structure of zintl compounds has a low lattice thermal conductivity about 1 W/mK [7, 8]. This zintl compounds contains a balanced valence combination of both ionically and covalently bonded atoms. The mostly ionic cations donate electrons to the covalently bound anionic species. The covalent bonding allows higher mobility of the charge-carrier species than that found in purely ionic materials. The combination of the bonding types leads to complex structures with the possibility of multiple structural units in the same structure. A good example is the compound $Yb_{14}MnSb_{11}$ which contain $[MnSb_4]^{9-}$ tetrahedra, polyatomic $[Sb_3]^{7-}$ anions and isolated Sb^{3-} anions and Yb^{2+} cations-Fig. 6. This complex structure has a low lattice thermal conductivity 0.4 W/mK and ZT =1 at 900°C [7, 8].

For the circumventing the inherent materials conflict of a phonon glass with electron crystal properties is ti imagine a complex material with distinct regions providing different functions. An example is the compound $Ca_xYb_{1-x}Zn_2Sb_2$ with sheets of disordered cations between layers of covalently bound Zn-Sb.

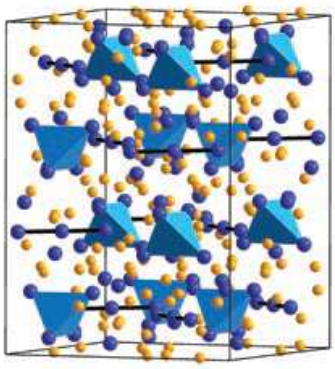

Fig. 6. The complexity of the $Yb_{14}MnSb_{11}$ unit cell is illustrated, with $[Sb_3]^{7-}$trimers, $[MnSb_4]^{9-}$ tetrahedra, and isolated Sb anions. The Zintl formalism describes these units as covalently bound with electrons donated from the ionic Yb^{2+} sublattice (yellow).

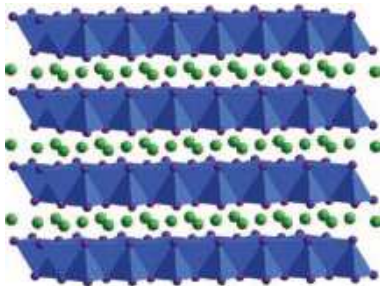

Fig. 7. $Ca_xYb_{1-x}Zn_2Sb_2$ structures both contain ordered layers (polyhedra) separated by disordered cation monolayers, creating electron-crystal phonon-glass structures.

$Ca_xYb_{1-x}Zn_2Sb_2$ demonstrates ability in the ionic layer concomitant with a modest reduction in lattice thermal conductivity due the alloying of Yb and Ca. The Ca^{2+} is slighly more electropositive than Yb^{2+}, which enables a gradual changing of the carrier concentration as the Yb/Ca ratio is changed. The doping produces disorder on the cation substructure, but not the conducting anion substructure such that the bandgap and carrier mobility is unchanged. The relative simple structure of $Ca_xYb_{1-x}Zn_2Sb_2$ leads to the relative high lattice thermal conductivity about 1.5 W/mK and a ZT>1, [7,8].

The nanostructured materials with precisely tailored size and shape are promising candidates for thermoelectric materials. The phonon scattering is optimized by controlling grain sizes, interfaces and chemical compositions. $PbSe_xTe_{1-x}$ quantum dot superlattice grown by molecular beam epitaxy (MBE) exhibit a ZT=1,6 and for Bi_2Te_3/Sb_2Te_3 superlattice obtained by MBE the ZT =2,4 [11]. The structure like n-type $AgPb_mTe_{2+m}$ and p-type $Na_{0.95}Pb_{20}SbTe_{22}$ prepared by high temperature solid-state yielding ZT values of 1.7 and 1.6 respectively [11]. Different film growth methods based on MBE, metallorganic chemical vapor deposition MOCVD, flash evaporation and coevaporation have been used to grow single layers and supperllatices on various substrate. For the system Bi_2Te_3/Sb_2Te_3 p-type supelattice exhibit a ZT=2.4 at room temperature and a power factor of 40 $\mu W/cmK^2$ [17]. The synthesis of nanowire PbX (X=S, Se, Te) including templating in mesoporous silica channel, oriented attachment of nanoparticles, seeded solution synthesis colloidal synthesis, solvothermal and hydrothermal and soft template routes. For the PbTe p-type nanowire was determined a resistivity of 0.1 Ω cm and a mobility of 0.71 $cm^2V^{-1}s^{-1.}$ [18].

IV. CONCLUSIONS

In summary, the paper presents a state-of–art about the bulk and nanostructured thermoelectric materials like Bi_2Te_3, Sb_2Te_3 , chalcogenides, zintl and skutterudites compounds, used in solid state thermoelectric generators, their synthesis method and the influence of crystalline structure about the performance like figure of merit , Seebeck coefficient, electrical and thermal conductivity. Also, was presented the theory of the thermoelectric generator function.

V. ACKNOWLEDGMENT

The Romanian National Authority for Scientific Research provided the support for this work through the project nucleus no. 5303/2012.

VI. References

[1] Qin Yao, Lidong Chen, Wenqing Zhang, Shengcong Liufu, Xihong Chen**, „**Enhanced Thermoelectric Performance of Single-Walled Carbon Nanotubes/Polyaniline Hybrid Nanocomposites", ACS Nano vol. 4, no. 4, (**2010)**, 2445-2451.

[2] Jefrey Snyder, "Small thermoelectric generators", Electrochemical Society Interface (**2008)**, 54-56.

[3] Strasser M., Aigner R., Franosch M., " Miniaturized thermoelectric generators based on poly-Si and poly-SiGe surface micromachining", Sensors and Actuators A, 97-98, 2002, 535-542.

[4] Basel I. Ismail, Wael H. Ahmed, „Thermoelectric Power Generation Using Waste-Heat Energy as an Alternative Green Technology", Recent Patents on Electrical Engineering (**2009)**, 2, 27-39.

[5] Wulf Glatz, Simon Muntwyler, Christofer Hiero, „Optimization and fabrication of thick flexible polymer based micro thermoelectric generator", Sensors and Actuators A 132 (2006) 337–345.

[6] Dewel Jia, Jing Liu, " Human power based enrgy harvesting strategies for mobile electronic devices", Front. Energy Power Eng. China, 3(1), 2009, 27-46.

[7] G. Jeffrey Snyder, Eric Toberer, "Complex thermoelectric materials", Mature Materials Nature Materials, vol. 7 **(2008),** 105-114.

[8] Susan M. Kauzlarich, Shawna R. Brown, G. Jeffrey Snyder, "Zintl phases for thermoelectric devices", Dalton Trans. (**2007)**, 2099-2107.

[9] Nidhi Dubey, Mario Leclerc, „Conducting Polymers: Efficient Thermoelectric Materials", Journal of Polymer Science Part B: Polymer Physics 49, (**2011)**, 467–475.

[10] Yugi Hiroshige, Makoto Ookawa, Naoki Toshima, " Thermoelectric figure of-merit of iodine-doped copolymer of phenylenevinylene with dialkoxyphenylenevinylene", Synthetic Metals 157 **(2007**) 467-474.

[11] Maksym V. Kovalenko, Boris Spokoyny, Jong-Soo Lee, Marcus Scheele, Andrew Weber, Susanthri Perera, Daniel Landry, and Dmitri V. Talapin," Semiconductor Nanocrystals functionalized with Antimony Telluride Zintl Ions for Nanostructured Thermoelectrics", J. Am. Chem. Soc., 132, (**2010)**, 6686–6695.

[12] Rowe. D. M., CRC Handbook of Thermoelectrics: Micro to Nano, Boca Raton, FL: CRC Press, **2005.**

[13] Baoling Huang, Chris Lawrence, Andrew Gross, Gi-Suk Hwang, Nilaufar Ghafouri, Sang-Woo Lee, Hanseup Kim, Chang-Peng Li, Khalil Najati, Massoud Kaviany, " Low-temperature characterization and micropatterning of coevaporated Bi_2Te_3 and Sb_2Te_3 films", Journal of Applied Physics, 104, (**2008**), 113710.

[14] L.M. Goncalvers, J.G. Rocha, C. Couto, P. Alpuim, J.H. Correia, "On-chip of thermoelectric Peltier microcoolers, " Sensors and Actuators A 145-146, (**2008)**, 75-80.

[15] Fistein Prytz, Electronic structure and bonding in thermoelectric skutterudites", University of Oslo, **2007.**

[16] Ctirad Uher, Chang-Peng Li, Sedat Ballikaya, „Charge compensed n-type skutterudites", Journal of Eletronic Materials, vol. 39, No. 9, **(2010)**, 2122-2126.

[17] H. Bottner, G. Chen, R. Venkatasubramanian, „Aspects of thin superlattice thermoelectric materials, devices and applications", MRS Bulletin, vol. 31, **(2006),** 211-217.

[18] Melissa Fardy, Allon I. Hochbaum, Joshua Goldberger, Minjuan Zhang, Peidong Yang, „Synthesis and thermoelectrical characterization of lead chalcogenide nanowire," Advanced Materials 19, **(2007)** 3047-3051.

VII. BIOGRAPHIE

Gabriela Telipan was born in Bucharest on November 19, 1957. He graduated at 1982 of Bucharest Polytechnic University and she is PhD Student at the Bucharest University Chemical Faculty. His employment experience included the National Research Electrical Engineering Institute, Dep. of Electrical Micromachines The research activity include: gas and air relative humidity sensors made by thin and thick technology.

THERMAL AND RADIATION STABILITY OF POLYOLEFINS MODIFIED WITH SILICA NANOPARTICLES

[*]Traian Zaharescu, [*]Ilona Plesa
*Research and Development National Institute of Electrical Engineering (INCDIE ICPE-CA), Splaiul Unirii, No. 313, District 3, 030138, Bucharest, Romania, zaharescut@yahoo.ro

Abstract - The effects of γ-irradiation as the accelerated degradation procedure were analyzed for the evaluation of material stability. Low density polyethylene, polypropylene and ethylene-propylene terpolymer were studied in formulations with SiO_2 nanoparticles (2 and 5 wt.%) or as neat samples. The exposure to high energy radiation (up to 100 kGy) has revealed a faster increase of carbonyl band than it was happened with hydroperoxide band, confirming the conversion of alkoxy intermediates into carbonyl compounds. Isothermal chemiluminescence determinations on thermal stability of samples indicate an increased resistance to oxygen attack of nonirradiated composites, while radiolysed materials containing nanofiller exhibit higher rate oxidation. Nonisothermal chemiluminescence investigations on all compositions two peaks at different temperatures, which demonstrate the accumulation of certain peroxy structures being further decayed. The three studied materials present increased oxidation rates with the received energy from incidental rays because the thermal regime of degradation depends on the structural characteristics, namely initial number of tertiary carbon atoms, unsaturation level. Electrical measurement of currents in all samples were recorded for the evaluation of radiation consequences on insulating properties. The fate of hydroperoxides as oxidation initiators is discussed.

I. INTRODUCTION

This document provides an example of the desired layout for a published MNE technical paper and can be used as a Microsoft Word template. It contains information regarding desktop publishing format, type sizes, and typefaces. Style rules are provided that explain how to handle equations, units, figures, tables, abbreviations, and acronyms. Sections are also devoted to the preparation of acknowledgments, references, and authors' biographies. The stability of composites consisting of polymers and nanophase is an intensively studied topic [1-10] because of the enormous number of applications recommended by their appropriate features. The most important of such effects are changing matrix properties, when nanoparticles of filler are present through polymer macromolecules [11]. The amplitude of modifications caused by the presence of nanocomponent in composites is determined by the enormous interphase area. The compatibilization between host polymer and inorganic material can be ensured by different modifiers, which reduce the superficial tension between components [12]. The most important problem of these nanocomposites is their durability, which characterizes the integrity of materials and their long term service. The thermal degradation of hybrid nanocomposites may starts by the segmental scissions or by physical interaction between polymer and inorganic constituent [13]. The molecule fragmentation as the result of energy depositing from incidental radiation is accompanied by the reactions of free radicals with diffused oxygen, whose rate depends on the filler concentration [14, 15]. It is often reported that nanoparticles play the role of scavenger for free radicals with the direct consequence of degradation rate [16]. The transfer of energy into polymer matrix causes the molecular splitting by the

break of weak bonds. The oxidation is an autocatalytic process which starts with the reactions of free radicals with molecular oxygen. The rate of propagation depends on the intensity of stressor, the duration of action and also on the mobility of intermediates [17]. However, the buildup and decay of hydroperoxides decide the kinetics of oxidative degradation, which may occur according with different schemes [18].

The durability of polymer materials, which determines the selection of usage areas, is properly assessed by accelerated degradation produced during high energy exposure, because the density of reactive entities is high enough for depicting material deterioration [19]. The material qualification by γ-irradiation is a confidence procedure which allows the evaluation of long-term resistance in connection with the operation in foreseen limit conditions [20]. The results collected from this kind of investigations are useful not only for nuclear energy industry, but also for various applications, where intensive oxidative degradation is expected.

This paper analyses comparatively the stability of polyethylene (LDPE), polypropylene (PP) and ethylene-propylene terpolymer (EPDM) modified by the presence of silica nanoparticles and subjected to γ-radiation for fast ageing.

II. EXPERIMENTAL

A. Materials

Low density polyethylene was produced by ROMPETROL PETROCHEMICALS (Romania) as type B 21/2 with the following characteristics: density – 0.9077 $g.cm^{-3}$, crystallinity – 42 %, melting index 3.25 g/10 min (190 ^{0}C/2.16 kg), number of CH_3 per 100 carbon atoms – 3.05. Polypropylene was purchased from ROMPETROL PETROCHEMICALS (Romania) as type TATREN HG 10.07. Its main features are: density – 0.8994 $g.cm^{-3}$, melting index 1.498 g/10 min (190 ^{0}C/2.16 kg). Ethylene-propylene diene rubber (EPDM) was purchased from ARPECHIM Piteşti (Romania), whose ethylene/propylene ratio was 3/2. The diene, ethylidene 2-norbornene (EBN), was initially in the concentration of 3.5 phr. All polymeric materials were used as received products. SiO_2 nanoparticles were manufactured by Degussa, as fumed silica, Aerosil 380, 100% purity, specific surface 380 $m^2.g^{-1}$, particle diameter range 3 – 15 nm.

B. Sample preparation and irradiation

Three levels of nanofiller concentration (0, 2 and 5 wt.%) were selected for the explanation of the effects induced by nanoparticles on the thermal behavior of material. These concentrations correspond to the usual compositions that do not drastically drop the mechanical properties of prepared nanocomposites.

Films (100 μm thickness) and sheets (0.5 mm thickness) were obtained by mixing basic polymer and nanofiller (SiO_2) in a Brabender Plastograph for 15 minutes at 180 ^{o}C. Specimens were pressed at 180 bars in an electrical device for 10 minutes after a preheating for 15 minutes. The pressing temperatures applied for sample preparation are listed in Table 1.

Table I. Pressing temperatures for sample preparation.

Polymer	Pressing temperature (^{o}C)		
	neat	2 %	5 %
EPDM	155	170	180
LDPE	120	150	165
PP	170	180	180

The exposure on radiochemical processing was performed in air at room temperature inside of a γ-irradiator M-38 GAMMATOR (USA), which has a ^{137}Cs source. The dose rate is 0.4 $kGy.h^{-1}$. Our composite samples covered with aluminum foil destined to the conversion of γ-rays into δ-electrons for a more efficient energetic transfer were continuously rotated for

homogenous irradiation. The values of received γ-dose were 0, 10, 20, 50 and 100 kGy.

C. Measurements

Chemiluminescence (CL) determinations were carried out with LUMIPOL 2 (Slovakia) device. The measurement temperature for isothermal regime was 190^{o}C, which ensures convenient degradation rate. The Chemiluminescence procedure for isothermal measurements was previously reported [21]; the nonisothermal experiments were carried out according with the method describe by Rychlý et al. [22]. This equipment maintains constant temperature with an error of ± 0.2 ^{o}C for the accomplishment of isothermal measurements, while the rate of heating for nonisothermal assays was selected as optimal value of 2 ^{o}C.min^{-1}. Thin small strips with thickness of 30 μm avoiding self-absorption of expelled photons were cut from initial sheets by means of a microtome. Sample was around 3 mg were posted on an aluminum tray, which does not affect the thermal stability of polymer degradation. JASCO 4200 spectrophotometer was used for FTIR records. The number of scans was 50, which provides a satisfactory resolution (4 cm^{-1}). The oxidized films were analyzed immediately to minimize the post γ-effect.

The absorption currents were recorded with an electrometer Keithley 6517A, connected with a Keithley 8009 test fixture and with a computer. The sample was placed between the two plane electrodes of the test fixture and a voltage step of 1000 V was applied to each sample during 60 minutes. The current variations were recorded for 60 minutes starting from the voltage application. For each sample one thousand values of the absorption current were recorded, each at every 3.6 seconds. All the measurements were performed at ambient temperature (27 ºC) and humidity (≈ 50 %). The nanocomposite samples for electrical tests performed in this study were plaques of square shape (10 x 10 cm^2) having the thickness of 0.5 – 0.6 mm.

III. DISCUSSION

Thermal and radiochemical oxidation processes are the result of the attack of oxygen onto macromolecules still during the induction period, when peroxyl radicals start to be formed as the initiators of degradation [23]. The oxidation scheme is presented in Fig. 1. The influence of molecular structure on the material stability may be evaluated by the measurement of end-product accumulation and kinetic parameters like induction period or oxidation rate, which depict the strength of molecules on bond scission. The practical question of the depth of structural modifications involves two major problems. The first one is the long-term exposure of polymer material to environmental attack accompanied by the accumulation of oxidation end-products. The second one is the confidence limits that are related to the operation of equipments where they are inserted. All the oxidative degradation products are linked by the rate of molecular oxygen diffusion into material, which dominated the physical process prior chemical reactions [24, 25]. According with the presented basic scheme for the oxidation of polyolefins, the degradation level can be evaluated by the assessment of oxygenated product content or by the analysis of material behavior under specific conditions. Complete approaches of the behavior of intermediates can be done either on detailed reactions of oxidation intermediates based on spectroscopic techniques [26] or on physico-chemical analysis like chemiluminescence [27].

A. FTIR spectroscopy analysis

The increase in the content of oxygenated compounds that are formed during radiolysis is presented in Table 2. The smooth growth of absorption for ethylene-propylene elastomer (EPDM) for the first 50 kGy would indicate the presence of a

light amount of stabilizer included in the pristine formulation. The presence of silica nanoparticles induces an accelerated oxidative degradation, which is intensified as dose enhances. The values of absorbance for ketone units are faster augmented than the similar values for hydroperoxides because either the consumption of ROOH (Fig. 1) by disproportion or the direct conversion of hydroperoxides into carbonyl compounds [28]. The higher amount of filler promotes oxidation probably due to the providing oxygen pre-adsorbed on the particle surface during sample preparation which was demonstrated by DSC investigations [29].

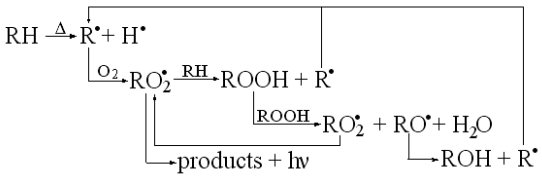

Figure 1. Oxidation scheme of polyolefins.

The slight differences between LDPE and PP regarding the intensities of 3350 cm^{-1} band can be noticed. The evolution of oxidation is connected with irradiation dose, which depicts the level of energetic transfer onto polymer molecules. The growing changes in transmission values start from the chain scission of polymer backbone that takes place rather at tertiary carbon atoms than any other sites. The accumulated dose leads to the asymptotic dependence of adsorption on irradiation dose attaining high figures at 100 kGy. The origin of the chain scission mechanism in polymers is the oxygen attacking the polymeric chain yielding alkoxy and peroxy radicals. These radicals abstract a hydrogen atom from the chain, giving rise to β scission, leading to a decrease in molecular weight and formation of carbonyl end groups [30].

Yang et al. demonstrated the contribution of various fillers on the oxidative degradation of high density polyethylene [31]. The similarity to our results emphasizes the added nanoparticles determines an diminution in the activation energy of oxidation degradation, which can be explained by the interaction of chemically linked oxygen atoms in nanoparticles and polymer macromolecules weakening some of their bonds (bond polarization). The progress in oxidation level, which is described by the ascendant extension of absorbance, must be correlated with the permeability of oxygen. It was found [32] that a higher permeability is caused by the presence of many small defects rather than a small number of large defects that are placed at boundary zones of polymer/nanoparticle interphase (Fig. 2). The exposure to γ-rays causes not only degradation, but also a slight crosslinking, which are simultaneously occurred. Low density polyethylene is known to be susceptible for radiochemical crosslinking, so that its oxidative degradation is slowed down; the measurable consequence is the smaller figures of absorbency that posts it as more stable polyolefins through the three polymers studied in this work.

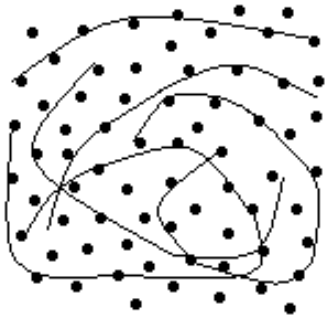

Figure 2. Spatial distribution of nanoparticles through macromolecules for adsorption/desorption equilibrium.

B. Isothermal chemiluminescence analysis

The oxidative degradation of polymers can be analyzed starting from isothermal chemiluminescence data [33, 34] by clear

depicting of different stages of oxidation. Fig. 3 presents the contribution of nanofiller on the thermal stability of polypropylene. This oxide promotes an adsorption process of free radical that delays material oxidation. The higher the concentration of nanofiller, the more efficient stability is obtained. The oxidation rates of these polypropylene formulations are visibly different that nanoparticles act as radical scavengers. The improvement in the thermal stability of polyerthylene and polypropylene by addition of nanoclay was previously reported by thermogravimetric analysis [35]. The order of thermal stability of studied polymers for each level of silica concentrations is confirm as LDPE > EPDM > PP, due to the unlike content of tertiary carbon atoms. The various shoulders appeared in the CL curves would be ascribed to the selective desorption of radicals of different sizes which have been trapped by nanoparticles. The height of CL maximum intensity decreases as the silica content is higher explaining the slower release of reactive units at higher concentration of nanofiller.

During the γ-irradiation of studied composite materials molecular scissions took place with different amplitude because of the dissimilar structures. The values of CL intensities depict the radiation stability of basic polymer. Polyethylene is a radiation stable material, whereas polypropylene and ethylene-propylene terpolymer are easily degraded in radiation field (Table 3) illustrates the deep discrepancy between these three polymers.

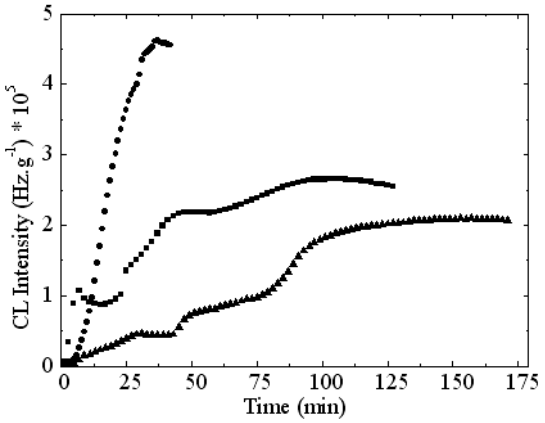

Figure 3. CL curves recorded on nonirradiated polypropylene samples at 190oC.
(,) pristine PP formulation; (!) PP modified with 2 %wt. SiO2 nanoparticles; (▲) PP modified with 5 %wt. SiO2 nanoparticles.

Table II. Absorbances of polyolefins modified with silica nanoparticles.

Dose	EPDM			LDPE			PP		
(kGy)	0	2	5	0	2	5	0	2	5
3350 cm^{-1} band									
0	3	6	6	4	5	8	3	6	6
10	3	7	7	5	6	13	3	6	8
20	5	9	8	6	7	14	4	6	10
50	7	11	9	7	8	16	8	8	15
100	10	11	11	11	11	18	16	21	21
1714 cm^{-1} band									
0	1	1	1	1	2	14	2	10	16
10	4	2	3	2	5	18	2	14	17
20	8	7	9	6	10	21	4	20	20
50	14	18	20	16	20	33	12	29	29
100	23	31	33	39	43	51	24	48	49

The CL emission of polyethylene growths smoothly, because this material is subjected to a thermal degradation initiated by the pre-existent peroxyl radicals and this infection 7 (Fig. 4a). Polypropylene is quickly degraded due to the unfavorable structural configuration comprising one tertiary carbon atom in each propylene

monomer unit. The other two polymers exhibit maxima on their CL curves, those noted for EPDM being much closer to intensity axe than shoulders noticeable for PP. The short time appearance of these maxima can be explained by the existence of a certain unsaturation brought by the constitutive diene. These double bonds are priory broken increasing the amount of peroxyl radicals. Polypropylene presents two maximum intensities (Fig. 4b) that can be caused by the two types of scissions: one homolytic bond between two neighbor carbon atoms (347 $kJ.mol^{-1}$) and the heterolytic bonds between carbon and hydrogen atoms (414 $kJ.mol^{-1}$) leading to different hydroperoxide structures. The flat development of oxidation of PP irradiated at 50 kGy is in a strike contrast with the progress in the degradation profiles of PP-based composites, which present a sharp increase of CL intensity. This feature is the consequence of the expelling of reactive intermediates from nanoparticle surface. The descendant shapes of CL curves for irradiated ethylene-propylene elastomer (EPDM) follow the early maxima (Fig. 4c), where free radicals were already decayed. On these curves the second CL intensity maximum is observed after about 120 minutes, whereas the similar values are recorded after 30-40 minutes, that indicates a higher stability of elastomer in comparison with polypropylene.

The noticeable differences between the CL emission measured for the n-SiO_2 composites of the three studied polyolefins can be the result of the unlike manners in the rates of free radical generation, in the adsorption /desorbtion equilibrium, in the diffusion rate of oxygen.

The numbers of molecular scissions found in the degrading polyethylene, polypropylene and ethylene-propylene rubber augment as the exposure time is extended. The corresponding distribution of free radicals and, consequently, oxidation end-products is correlated to the action of filler nanoparticles; nanoparticles act as a source of radicals, which had been formed during radiolysis [36, 37].

C. Nonisothermal chemiluminescence analysis

The kinetic aspects of generation and decay of hydroperoxides have been extensively reported [38-41]. The yields of hydroperoxides obtained in polyethylene and polypropylene after controlled oxidation under freezing [42]. Unfortunately, there are not references on the different structures of hydroperoxides that ate formed during radiolysis. The activation energies for the decomposition of hydroperoxides are placed in a large value range (80-140 $kJ.mol^{-1}$ [43]. The low thermal stability of hydroperoxides stated of the low value of O – O bond (150 $kJ.mol^{-1}$) [44] may explain the initiation of oxidation chain during and after radiolysis of polyolefins.

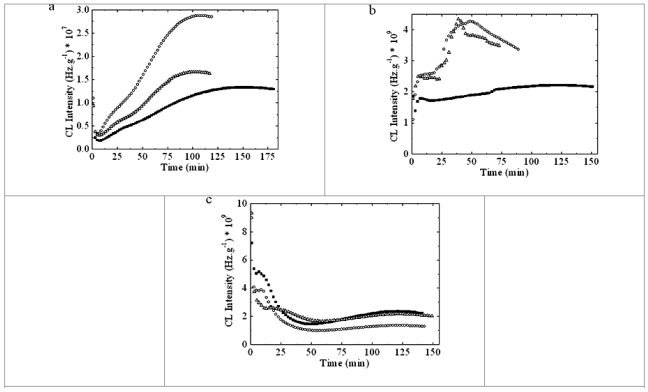

Figure 4. Isothermal chemiluminescence curves recorded at 190oC for thermal oxidation of nonirradiated polyolefin samples. (a) LDPE; (b) PP; (c) EPDM. (!) pristine polymer; (○) 2 wt.% silica; (8) 5 wt.% silica.

The nonisothermal curves recorded for all sample compositions are presented in Figs. 5-7. The progress in the oxidation degradation looks unlike for the three studied polyolefins. The polyethylene samples with or without nanofiller present two maxima of CL intensity, one at 98 ^oC and the other one at 158 ^oC, more

prominent for neat and 2 %wt. SiO_2 samples. For ethylene-propylene terpolymer two CL emission maxima are also noticed at 98 ^oC and at temperatures around 200 ^oC or higher. Polypropylene exhibits one maximum intensity peak around 200 ^oC for samples which were received more than 20 kGy. As it was previously reported for the formation of hydroperoxides in polyacrylonitrile, two CL emission maxima appear when this polymer is nonisothermally heated in nitrogen [45]. According with the mechanism reported for the consumption reactions involving hydroperoxides [44], the most part of ROOH participates in bimolecular reaction:

$$POOH + POOH \longrightarrow POO^{\bullet} + PO^{\bullet} + H_2O$$

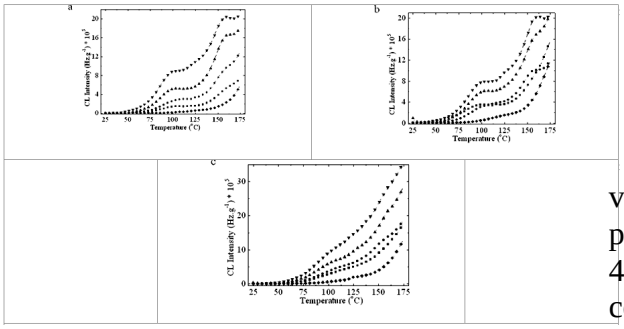

Figure 5. Nonisothermal chemiluminescence curves recorded on LDPE composites irradiated at different doses.
(a) pristine sample; (b) 2%wt. silica (c) 5 %wt.silica.
(◆) 0 kGy, (!) 10 kGy, (,) 20 kGy, (▲) 50 kGy, (▼) 100 kGy.

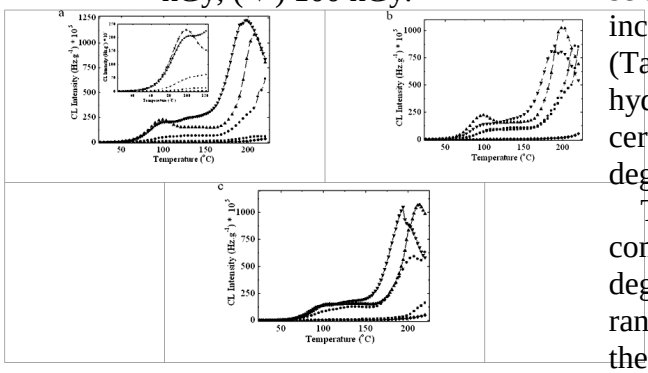

Figure 6. Nonisothermal chemiluminescence curves recorded on EPDM composites irradiated at different doses. (a) pristine material; (b) 2%wt. silica (c) 5 %wt. silica. The meaning of marks is the same as in Fig. 5.

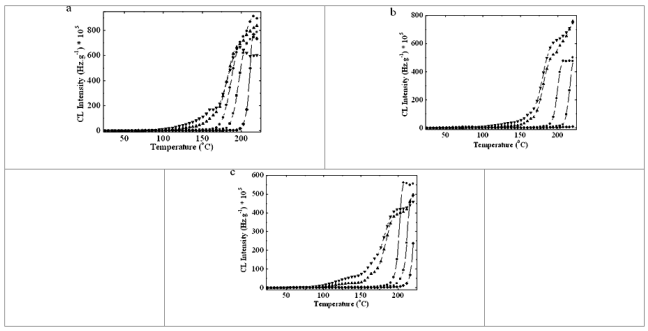

Figure 6. Nonisothermal chemiluminescence curves recorded on PP composites irradiated at different doses.
(a) pristine material; (b) 2%wt. silica (c) 5 %wt. silica. The meaning of marks is the same as in Fig. 5.

The theoretical bond enthalpies for various hydrocarbon model compounds are placed on two distinguish ranges: around 400 $kJ.mol^{-1}$ and 150 $kJ.mol^{-1}$. They correspond to the following structures: ROO-H and *t*-C_4H_9O-H for the first group, and $(CH_3)_3CO$-$OC(CH_3)_3$ together with *t*-C_4H_9O-OH for the second group. These values of enthalpy are correlated with the decrease in the CL emission intensity as the consequence of decay of hydroperoxides. It means that the existence of tertiary configurations can be proved and the β-scission of alkoxy radicals leads to an increased amount of carbonyl compounds (Table 2). The thermal decomposition of hydroperoxides is tightly related to the certain intermediates that depict the degradation route.

The presence of SiO_2 nanofiller in our composites delays the oxidative degradation especially on the low dose range. At superior doses exceeding 50 kGy, the oxidation occurs faster in polypropylene than in polyethylene and ethylene-

propylene terpolymer. The propagation of oxidation takes place by hydrogen abstraction by peroxyl radicals, alkoxy structures and trans-vinylene [46].

C. Electrical behavior

The answers of investigated composite to the action of ionizing radiation are listed in table 4. The satisfactory values of volume resitivities recommend them for the manufacture of cable insulations, even at 1000 V regime.

Table III. Volume resitivities of studied composites measured at 1000V.

Polymer material	Filler concentration (%)	Dose (kGy)	Volume resistivity (□.m)
EPDM	0	0	$9.22 \cdot . 10^{15}$
		10	$5.47 \cdot . 10^{15}$
		20	$9.75 \cdot . 10^{14}$
		50	$2.93 \cdot . 10^{15}$
	2	0	$2.88 \cdot . 10^{16}$
		10	$3.28 \cdot . 10^{16}$
		20	$2.88 \cdot . 10^{16}$
		50	$2.14 \cdot . 10^{16}$
	5	0	$2.88 \cdot . 10^{16}$
		10	$3.28 \cdot . 10^{16}$
		20	$2.88 \cdot . 10^{16}$
		50	$2.14 \cdot . 10^{16}$
LDPE	0	0	$3.00 \cdot 10^{16}$
		10	$4.88 \cdot . 10^{14}$
		20	$5.79 \cdot . 10^{14}$
		50	$1.03 \cdot . 10^{14}$
	2	0	$3.60 \cdot . 10^{14}$
		10	$2.97 \cdot . 10^{14}$
		20	$9.52 \cdot . 10^{14}$
		50	$2.18 \cdot . 10^{14}$
	5	0	$5.83 \cdot . 10^{15}$
		10	$2.84 \cdot . 10^{15}$
		20	$1.98 \cdot . 10^{15}$
		50	$5.57 \cdot . 10^{14}$
PP	0	0	$8.73 \cdot . 10^{16}$
		10	$1.15 \cdot . 10^{16}$
		20	$8.04 \cdot . 10^{15}$
		50	$2.07 \cdot . 10^{16}$
	2	0	$1.10 \cdot . 10^{16}$
		10	$5.44 \cdot . 10^{15}$
		20	$1.19 \cdot . 10^{16}$
		50	$1.16 \cdot . 10^{16}$
	5	0	$1.33 \cdot . 10^{15}$
		10	$7.93 \cdot . 10^{14}$
		20	$1.07 \cdot . 10^{15}$
		50	$1.02 \cdot . 10^{15}$

In function of practical requirements, the insulation manufacturers can select one of these compositions, which exhibits good values for electrical conduction. The correlation between chemical modification and the dose dependence of electrical properties may decide the range of applications.

IV. Conclusions

The characterization of thermal stability for polyethylene (LDPE), polypropylene (PP) and ethylene-propylene terpolymer (EPDM) modified with certain amounts of SiO_2 nanoparticles emphasizes the involvement of filler in the degradation mechanism through adsorption/desorption equilibrium, as well as through the modification of the generation rates of hydroperoxides. The material behavior is consistent with the polymer structure, which reveals the weak positions of tertiary carbon atoms. It was expected that nanofiller acts as a radical scavenger and the delaying in oxidative degradation is the result of interaction between nanoparticles and polymer macromolecules. The FTIR assay pointed out the higher rate of carbonyl accumulation and the slight differences between the absorbances of composites with the same basic polymer.Appendixes, if needed, appear before the acknowledgment.

V. References

[1] M. Abdelwahab, T. Agag, A. Akelah, and T. Takeichi, *Polym. Eng. Sci*., **52**, 125 (2012).

[2] N.Tz. Dintcheva, F.P. La Mantia, and V. Malatesta, *eXPRESS Polymer Letters*, **5**, 923 (2011).

[3] S. C. Tjong and Y. W. Mai, *Polymer Nanocomposites: Physical Properties and Applications*, Woodhead Publishing House, 2010.

[4] J. Díez, L. Barral, R. Bellas, R. Bouza, J. López, C. Marco, and G. Ellis, *Polym. Eng. Sci*., **51**, 1720 (2011).

[5] P. Santamaría, J.I. Eguiazábal, and J. Nazábal, *J. Appl. Polym. Sci*., 116, 2374 (2010).

[6] R.F. Gibson, *Composite Structures*, **92**, 2793 (2010).

[7] E. Manias, J.G. Zhang, J.Y. Huh, K. Manokruang, P. Songtipya, and M. Jimenez-Gasco, *Macromol. Rapid Commun*., **30**, 17 (2009).

[8] A. Leszczyńska, J. Njuguna, K. Pielichowski, and J. R. Banerjeec, *Thermochim. Acta*, **454**, 1 (2007).
[9] J.G. Zhang, and C. A. Wilkie, *Polymer*, **47**, 5736 (2006).
[10] T. Zaharescu, S. Jipa, W. Kappel, and P. Supaphol, *Macromol. Symp*., **242**, 319 (2006).
[11] L. Százdi, A. Pozsgay, and B. Pukánszky, *Eur. Polym. J.*, **43**, 345 (2007).
[12] J.K. Pandey, K. Raghunatha Reddy, A. Pratheep Kumar, and R.P. Singh, *Polym. Degrad. Stab*., **88**, 234 (2005).
[13] A.D. Drozdov, *Eur. Polym. J.*, **43**, 1681 (2007).
[14] I.C. Finegan, G.G. Tibbetts, and R.F. Gibson, *Compos. Sci. Technol.*, **63**, 1629 (2003).
[15] V. Vladimirov, C. Betchev, A. Vassiliou, G. Papageorgiou, and D. Bikiaris, *Compos. Sci. Technol*., **66**, 2935 (2006).
[16] T. ZAHARESCU, S. JIPA, AND P. SUPAPHOL, *POLYM. BULL.*, 64, 783 (2010).
[17] A. Chatterjee, and B.L. Deopura, *J. Appl. Polym. Sci.*, **100**, 3574 (2006).
[18] E. Richaud, X. Colin, B. Fayolle, L. Audouin, J. Verdu, *J. Chem. Kinet.*, 40, 769 (2008).
[19] T. Zaharescu, L. Andrade e Silva, S. Jipa, and W. Kappel, *Radiat. Phys. Chem.*, **79**, 388 (2010).
[20] S. Cheng, E. Phillips, and L. Parks, *Radiat. Phys. Chem.*, **78**, 563 (2009).
[21] S. Jipa, T. Zaharescu, R. Setnescu, T. Setnescu, M.J.S. Brites, A.M.G. Silva, M.J. Marcelo-Curto, and B. Gigante, *Polym. Int*., **48**, 414 (1999).
[22] L. Matisova-Rychla, and J. Rychlý, *J. Polym. Sci.*, **42**, 648 (2004).
[23] T. Zaharescu, M. Giurginca, and S. Jipa, *Polym. Degrad. Stab*., **63**, 245 (1999).
[24] K.T. Gillen, and R.L. Clough, *Prediction long-term mechanical performances of polymer*, in D.W. Clegg and A.A. Collyer (eds.) Irradiation Effects on Polymers, Elsevier, 157 (1991).
[25] E. Richaud, F. Farcas, B. Fayolle, L. Audouin, and J. Verdu, *Polym. Degrad. Stab*., **92**, 118 (2007).
[26] J.C.W. Chien, and H. Jabloner, *J. Polym. Sci., Part A1*, **6**, 393 (1963).
[27] M. Koutný, T. Václavková, L. Matisová-Rychlá, and J. Rychlý, *Polym. Degrad. Stab*., **93**, 1515 (2008).
[28] F. Gugumus, *Polym. Degrad. Stab*., **77**, 147 (2002).
[29] M. Modesti, A. Lorenzetti, D. Bon, and S. Besco, *Polym. Degrad. Stab*., **91**, 672 (2006).
[30] D.M. Mowery, R.A. Assink, D.K. Derzon, S.B. Klamo, R. Bernstein, and R.L. Clough, *Radiat. Phys. Chem*., **76** 864 (2007).
[31] R. Yang, Y. Liu, J. Yu, and K.H. Wang, *Polym. Degrad. Stab*., **91**, 1651 (2006).
[32] S. Mrkić, K. Galić, M. Ivanković, S. Hamin, and N. Ciković, *J. Appl. Polym. Sci*., **99**, 1590 (2006).
[33] J. Pospíšil, Z. Horák, J. Pilař, N.C. Billingham, H. Zweifel, and S. Nešpůrek, *Polym. Degrad. Stab.*, **82**, 145 (2003).
[34] L. Matisova-Rychlá, J. Rychlý, and K. Slovák, *Polym. Degrad. Stab.*, **82**, 173 (2003).
[35] J.G. Zhang, D.D. Jiang, and C.A. Wilkie, *Polym. Degrad. Stab.*, **91**, 641 (2006).
[36] T. Zaharescu, M. Kaci, R. Setnescu, S. Jipa, N. Touati, *Polym. Bull*., 56, 405 (2006).
[37] A.V. Shyichuk, J.R. White, I.H. Craig, and I.D. Syrotynska, *Polym. Degrad. Stab*., **88**, 415 (2005).
[38] F. Gugumus, *Makromol. Chem., Macromol. Symp*., **27**, 25 (1989).
[39] N.C. Billingham, E.T.H. Then, and P.J. Gijsman, *Polym. Degrad. Stab.*, **34**, 263 (1991).
[40] L. Zlatkevich, *Polym. Degrad. Stab.*, **83**, 369 (2004).
[41] N.C. Billingham, and M.N. Grigg, *Polym. Degrad. Stab.*, **83**, 441 (2004).
[42] Yu.A. Shlyapnikov, T.A. Bogaevskaya, S.C. Kiryushkin, and T.V. Monakhova, *Eur. Polym. J*., **15**, 737 (1979).
[43] N.V. Zolotova, and E.T. Denisov, *J. Polym. Sci., Part A1: Polym. Chem.*, **9**, 3311 (1971)
[44] E. Richaud, F. Farcas, B. Fayolle, and L. Audouin, J. Verdu, *Polym. Testing*, **25**, 829 (2006).
[45] L.T. Memetea, N.C. Billingham, and E.T.H. Then, *Polym. Degrad. Stab*., **47**, 189 (1995).
[46] M. Coquillat, J. Verdu, X. Colin, L. Audouin, and R. Nevière, *Polym. Degrad. Stab*., **92**, 1334 (2007).

VI. BIOGRAPHIES

Traian Zaharescu was graduated on 1965 at the Faculty of Chemistry, University of Bucharest. The PhD thesis was presented on the area of thermodynamics of His career followed activities in nuclear fuel elements, chemistry of materials for electrical engineering, radiation chemistry for durability characterization, educational performances teaching on modification of polymers under high energy irradiation. His expertise covers complementary areas like modification induced by ionizing radiation, chemistry of electrical engineering, aeronautic and nuclear materials. The published several papers and books on the materials science branch are related to the degradation and stabilization of polymers, physical, chemical and electrical which depict on structural changes induced by polymerization, ageing and recycling.

Ilona PLESA was born in Valenii de Munte, Romania, on February 6, 1983. She received the B.S. in electrical engineering in 2006, from the "Politehnica" University of Bucharest (PUB), Bucharest, Romania. In February 2012 she defended the PhD thesis on the influence of inorganic nanofillers on dielectric properties of polymer nanocomposites based on polyethylene, sustained by PUB.

She is currently a Research Assistant in the Department of Advanced Materials of the National Institute for Research and Development in Electrical Engineering, ICPE-CA, Bucharest, Romania. Hers main interests are in the following fields: dielectric properties of polymeric nanocomposites, dielectric spectroscopy, numerical modeling of phenomena in nanodielectrics.

Preparation of a Formatted Technical Paper for the Bulletin of Micro and Nanoelectrotehnologies

*Alexandru-Laurentiu Catanescu, **George Claudiu Zarnescu
Research and Development National Institute of Electrical Engineering (INCDIE ICPE-CA),
Splaiul Unirii, No. 313, District 3, 030138, Bucharest, Romania, *catanescu@icpe-ca.ro,

Abstract - This document is itself an example of the desired layout (inclusive of this abstract) and can be used as a template. The document contains information regarding desktop publishing format, type sizes, and typefaces. Style rules are provided that explain how to handle equations, units, figures, tables, abbreviations, and acronyms. Sections are also devoted to the preparation of acknowledgments, references, and authors' biographies. The abstract is limited to 150 words and cannot contain equations, figures, tables, or references. It should concisely state what was done, how it was done, principal results, and their significance.

Index Terms **- The author shall provide up to 10 keywords (in alphabetical order) to help identify the major topics of the paper and to be enough referenced.**

I. INTRODUCTION

This document provides an example of the desired layout for a published MNE technical paper and can be used as a Microsoft Word template. It contains information regarding desktop publishing format, type sizes, and typefaces. Style rules are provided that explain how to handle equations, units, figures, tables, abbreviations, and acronyms. Sections are also devoted to the preparation of acknowledgments, references, and authors' biographies.

II. TECHNICALWORK PREPARATION

Please use automatic language check for your spelling. Additionally, be sure your sentences are complete and that there is continuity within your paragraphs. Check the numbering of your graphics (figures and tables) and make sure that all appropriate references are included.

A. Template

This document may be used as a template for preparing your technical paper. When you open the file, select "Page Layout" from the "View" menu (View | Page Layout), which allows you to see the footnotes. You may then type over sections of the document, cut and paste into it (Edit | Paste Special | Unformatted Text), and/or use markup styles. The pull-down style menu is at the left of the Formatting Toolbar at the top of your Word window (for example, the style at this point in the document is "Text"). Highlight a section that you want
to designate with a certain style, then select the appropriate name on the style menu.

B. Format

If you choose not to use this document as a template, prepare your technical work in single-spaced, double-column format, on paper A4 (21x29.7 centimeters). Set top, bottom margins and right margins to 15 millimeters and left margins to about 20 millimeters. Do not violate margins (i.e., text, tables, figures, and equations may not extend into the margins).

C. Typefaces and Sizes

Please use a Times New Roman font. (See your software's "Help" section if you do not know how to embed fonts.) Table I is a sample of the appropriate type sizes and styles to use.

TABLE I. Table name will be written in Times New Roman font.

Micromotor Code	b [mm]	a [mm]	h [mm]	Material
MPR33	33	25	20	PZT 5
MPR27	27	18	9	PZT 5
MPR15	16	10	10	PZT 5

D. Section Headings

A primary section heading is enumerated by a Roman numeral followed by a period and is centered above the text.
A primary heading should be in capital letters and bolded. The standard text format is considered times new roman 12.

The paper title should be in times new roman 20 uppercase and lowercase letters, not all uppercase.

Author name is set to times new roman 12, institution and contact address (E-mail) are set to times new roman 10.
Financial support should be acknowledged below the author name and institution. Example: This work was supported in part by the U.K. Department of Defence under Grant TX123.

A secondary section heading is enumerated by a capital letter followed by a period and is flush left above the section. The first letter of each important starting word is capitalized and the heading is bolded and italicized.

Tertiary and quaternary sections are accepted only in special cases, so usually must be avoided in order to keep a clear article structure. If required, a tertiary and quaternary section heading must be italicized and enumerated by adding an arabic numeral after each letter.

E. Figures and Tables

Figure axis labels are often a source of confusion. Try to use words rather than symbols. As an example, write the quantity "Torque," or "Torque, *M*," not just "*M*." Put units in parentheses. Do not label axes only with units. As in Fig. 1, write "Torque (cNm)" not just "(cNm)". Do not label axes with a ratio of quantities and units. For example, write "Current (A)," not "Current/A." Figure labels should be legible, approximately 10-point type.

Large figures and tables may span both columns, but may not extend into the page margins. Figure captions should be below the figures; table captions should be above the tables. Do not put captions in "text boxes" linked to the figures. Do not put borders around your figures.

All figures and tables must be in place in the text centered and written with times new roman 10. Use the abbreviation "Fig. 1" in sentence and for each figure name. Each table must be defined as „TABLE I”, with capital letters and roman numbers.

Digitize your tables and figures. To insert images in Word, use Insert | Picture | From File.

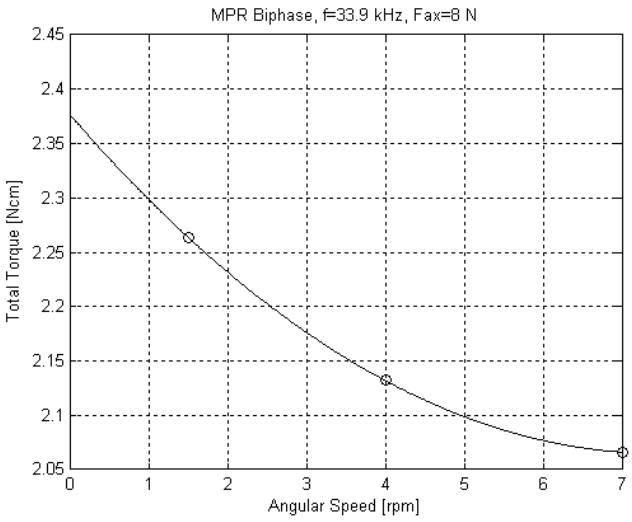

Fig. 1. Total torque function of angular speed. (Note that "Fig." is abbreviated and there is a space after the figure number.)

F. Numbering

Number reference citations consecutively in square brackets [1]. The sentence punctuation follows the brackets [2]. Multiple references [2], [3] are each numbered with separate brackets [1]-[3]. Refer simply to the reference number, as in [3]. Do not use "Ref. [3]" or "reference [3]"

except at the beginning of a sentence: "Reference [3] shows….".
Number footnotes separately with superscripts (Insert | Footnote). Place the actual footnote at the bottom of the column in which it is cited. Do not put footnotes in the reference list. Use letters for table footnotes.
Check that all figures and tables are numbered correctly. Use Arabic numerals for figures and Roman numerals for tables.
Appendix figures and tables should be numbered consecutively with the figures and tables appearing in the rest of the paper. They should not have their own numbering system.

G. Units

Metric units are preferred in light of their global readership and the inherent convenience of these units in many fields. In particular, the use of the International System of Units (“Système International d'Unités” or SI Units) is advocated. This system includes a subsystem of units based on the meter, kilogram, second, and ampere (MKSA). British units may be used as secondary units (in parentheses). An exception is when British units are used as identifiers in trade, such as 3.5-inch disk drive.

H. Abbreviations and Acronyms

Define less common abbreviations and acronyms the first time they are used in the text, even after they have been defined in the abstract. Standard abbreviations such as SI, CGS, AC, DC, and *rms* do not have to be defined. Do not use abbreviations in the title unless they are unavoidable.

I. Math and Equations

Use either the Microsoft Equation Editor or the *MathType* commercial add-on for MS Word for all math objects in your paper (Insert | Object | Create New | Microsoft Equation *or* MathType Equation). "Float over text" should *not* be selected.
To make your equations more compact, you may use the solidus (/), the exp function, or appropriate exponents. Italicize symbols for quantities and variables. Use a long dash for a minus sign or after the definition of constants and variables. Use parentheses to avoid ambiguities in denominators.
The number of each equation must be consecutively added in parentheses and arranged at the right margin, as in (1). Be sure that the symbols in your equation have been defined before the equation appears or immediately following.

Don’t use "Eq. (1)" abbreviation instead of "equation (1)," in a sentence.

$$L_m = \frac{m}{A^2} \quad (1)$$

With m – mechanical mass, A – force factor, L_m – Electromechanical inductance.

III. ACKNOWLEDGMENT

The following is an example of an acknowledgment.

The authors gratefully acknowledge the contributions of Mircea Ignat and Puflea Ioan for their work on the original version of this document.

IV. APPENDIX

Appendixes, if needed, appear before the acknowledgment.

V. References

References are important to the reader; therefore, each citation must be complete and correct. There is no editorial check on references, only the format times new roman 10 must be considered.

[1] Satanobu J., Lee D.K, Nakamura K., Ueha S., ”Improvement of the Longitudinal Vibration System for the Hybrid Transducer Ultrasonic Motor”, IEEE Trans. On Ultrasonic ferroelectrics and Frequency Control, vol. 47, no. 1, January 2000, pp. 216-220.
[2] Morita T., Yoshida R., Okamoto Y., Kurosawa M., ”A Smooth Impact Rotation Motor Using a Multi-Layered Torsional Piezoelectric Actuator”, IEEE Trans. On Ultrasonic ferroelectrics and Frequency Control, vol. 46, no. 6, November 1999, pp. 1439-1446.

• VI. BIOGRAPHIES

A technical biography for each author must be included. It should begin with the author's name (as it appears in the byline). Please do try to finish the two last columns on the last page at the same height. The following is an example of the text of a technical biography:

Mircea Ignat was born in Bucharest on March 4, 1953. He graduated at 1977 and he received Ph.D. degrees in electrical engineering from Bucharest Polytehnic University in 1999.

His employment experience included the National Research Electrical Engineering Institute, Dep. of Electrical Micromachines Research and he is the head of Electromechanics Department.

The research preoccupation include: the syncrone generators and the high speed electric machines. Is member of IEEE.

Equipment for investigation of mechanical characteristics of thin layers NHT, MHT+MST

Area of application:

Determining mechanical properties of thin layers of anorganic materials (metals, semiconductors, conductors, magnetic materials, DLC), organic materials (polymers, plastics, paints), ceramics, composite materials or biomaterials layered on cylindrical or paralelipipedical samples.

Functional parameters:

- nanoindentation module with working bench,
- microindentation and scratching module,
- control unit and software for data acquisition, storage and data processing and graphical data representation,
- dedicated software for characterization of indentation, scratching, adherence, elasticity module, CMX, DMA.

Equipment for tribological characterization of thin layers

Area of application:

Determination of tribological properties (wear and tear) of thin layers of anorganic materials (metals, semiconductors, conductors, magnetic materials, DLC), organic materials (polymers, plastics, paints), ceramics, composite materials or biomaterials layered on cylindrical or paralelipipedical samples by means of ball on disc tests or pin on disc with rotational or linear movement.

Functional parameters:

- main unit
  - ball-on-disk and pin-on-disk tribometer,
  - “dead weight” loading system in the range of: 0.25 … 38.75N,
  - 0.25N, 0.5N, 1N; 2N; 5N; 10N; 20N weights,
  - Rotative testing module, maximum speed: 1500rmp,

- Linear testing module, testing speed of max. 100mm/s,

- control unit with data acquisition and analysis
  - dedicated command, acquisition and data processing software: TriboX,
  - surface analysis software for wear profile determination, elastic modeling software ModelX, ASCII exportable data, measurement report generation,
- measurement system
  - friction force sensor (LVDT) $\leq$ 20N,
  - online measurement sensor for wear depth (RVDT),
  - humidity and temperature sensor,
  - curvature sensor,
  - electrical contact resistance sensor in the 0 … 1000Ω domain,
  - stylus profilometer for wear measurement,
  - high temperature room (Tmax=150°C) – for the rotational system.

Plasma source equipment for ultra-high void processing of materials through magnetron-sputtering and e-beam ATC 2200 AJA INTERNATIONAL

Area of application:

Fabrication of thin layers and nanostructures of conductive materials, resistive materials, oxidic semiconductors, insulators.

Functional parameters:

- minimal pressure $5x10^{-8}$ torr,
- evaporation working pressure $5x10^{-8}$ torr,
- vacuum dipstick: 760-510^{-9} torr,
- 4 sputtering sources for CC, pulsed CC and radio frequency,
- Electron beam evaporator for ultra high void (UHV) from 5 crucibles.

Ni spur, electrochemically deposited.